This is a non-peer-reviewed preprint submitted to EarthArXiv
This manuscript has been submitted to Geophysical Research Letters for peer review

Paleomagnetic data from the Qaidam Block quantify post-middle Triassic convergence preceding eastern Eurasian assembly

Ruiyang Chai[1,2]; Yanan Zhou[1*]; Douwe J. J. van Hinsbergen[2]; Teng Wang[1]; Qiang Fu[2,3]; Zhenwei Chen[1]; Chunxi Qu[1]; Shuqi Lan[1]; Xin Cheng[1]; Hanning Wu[1]

[1]State Key Laboratory of Continental Evolution and Early Life, Department of Geology, Northwest University, Xi'an, China

[2]Department of Earth Sciences, Utrecht University, Utrecht, Netherlands

[3]Institute of Earth Sciences, Heidelberg University, Heidelberg, Germany

[*]Corresponding author: Yanan Zhou (zhouyanan@nwu.edu.cn)

Key Points:

- A new Middle–Late Triassic (~240 Ma) paleomagnetic pole from the Qaidam Block indicates ~19° paleolatitudinal separation from Eurasia.
- The Qaidam and North China Blocks moved in unison, like part of a single, coherent plate, during the Triassic
- A cryptic, perhaps buried suture that accommodated major post-Triassic convergence, likely below the Tarim basin

Abstract

Amalgamation of East Asian blocks with Eurasia involved progressive closure of several oceanic basins preserved as sutures. Since the Permian, the North China Block has undergone ~2500 km of paleolatitudinal motion relative to Eurasia, forming Mongol–Okhotsk suture in the north. Surprisingly, no evidence in its western part has been found to coordinate this motion, which is essential for a triple conjunction with the suture. Here we report a new Middle Triassic paleomagnetic pole from the Qaidam Block, which connected the Tarim and North China Blocks, indicating a paleolatitude of ~35°N. This result is indistinguishable from coeval paleolatitudes of the North China Block, suggesting that both northward moved in unison as a coherent tectonic plate. Since the Tarim Basin had already been part of Eurasia, we propose that a cryptic, perhaps buried suture that accommodated post-Triassic convergence might be buried below the Tarim Basin or the NW Tibetan Plateau.

Plain Language Summary

The North China Block finally collided with Siberia in the Early Cretaceous, but its western boundary with the Tarim Block remains uncertain. Previous studies show that during the late Paleozoic to early Mesozoic, North China was located about 2,500 km south of Eurasia. Such a large northward movement requires closure of a major ocean. However, there is still no clear geological trace of this ocean that exists between the North China and Tarim Blocks. Given that the Qaidam Block forms a tectonic bridge between the Tarim and North China Blocks, we analyzed the paleolatitude of the Qaidam Block in the Middle Triassic to help resolve this puzzle. Our results show that a paleo-ocean still separated North China and Tarim during the Middle Triassic. The suture of this paleo-ocean is now buried beneath the Tarim Basin or the NW Tibetan Plateau, forming part of the system that completed the final amalgamation of eastern Eurasia.

1 Introduction

The final amalgamation of the Eurasian continent represents a pivotal process in northern hemisphere paleogeography and followed upon the closure of the Mongol-Okhotsk Ocean that intervened Siberia and an east Asian continental collage in the earliest Cretaceous (Dong et al., 2021, 2018; Eizenhöfer and Zhao, 2018; Metcalfe, 2021; Van Der Voo et al., 2015; Xiao et al., 2015). This collage consists of prominent continental fragments that had sutured together earlier, including the North China Block that connected with Amuria upon late Permian to early Triassic closure of the Solonker ocean (Eizenhöfer and Zhao, 2018). Reconstructing the paleogeographic and plate tectonic evolution of the closure of the last intra-Asian ocean is thus possible using paleomagnetic data from North China, as well as from further connected continental blocks. However, in contrast to the well-defined Mongol-Okhotsk suture (Jolivet et al., 2017; Wang et al., 2022a; Zhao et al., 2025), the location of the paleo-plate boundary that must also have been located somewhere between North China and the Tien Shan mountain belt to its west, where geological and paleomagnetic data show that the Tarim continental block collided with the rest of Eurasia in the Permian (Sharps et al., 1989; Wei et al., 2020, Xiao et al., 2020, 2013), remains unclear due to the absence of a clearly identified Mesozoic suture zone (Wang et al., 2025). Only in the southwest, early Cretaceous suturing within Eurasia is evident again from geological data of the Waser suture of Afghanistan and the western Rushan Pshart suture in the Pamir region (Yogibekov et al., 2023)

If suture zones are somehow stratigraphically or tectonically buried and become cryptic, locating them presents a plate kinematic challenge that may be benefit from collection of paleomagnetic data. Paleomagnetic data from the basins of North China Block revealed a N-S component of convergence of approximately 2500 km since the late Permian to Triassic period (Van Der Voo et al., 2015; Wang et al., 2025), enough to conclusively demonstrate within paleomagnetic uncertainty. Approximating the location of a cryptic suture may then occur through determining how far west rock units recorded paleolatitudes similar to those predicted from North China paleomagnetic data.

The Qaidam Block (QB) of Northern Tibet is located adjacent to the Tarim Basin and is separated from it by the active Altyn Tagh strike-slip fault. To the northeast, the Qaidam Block is separated from the Alxa block (that had been part of the North China Block since the Paleozoic (Sun and Dong, 2020; Zhang et al., 2016; Bu et al., 2020) by the Cenozoic intracontinental Qilian Shan-Nan Shan fold thrust belt that formed during Tibetan Plateau growth and that accommodated up to ~150 km of Cenozoic shortening (Van Hinsbergen et al., 2011; Zuza et al., 2016). There is no Mesozoic record of subduction or shortening in the Qilian Shan-Nan Shan region and Qaidam and North China thus could have been part of the same continent (Cocks and Torsvik, 2013; Huang et al., 2018; Wang et al., 2022b; Wang et al., 2025; Xiao et al., 2009). However, the missing, cryptic suture may also be located between North China and Qaidam with the latter being part of the Tarim Block since the late Paleozoic (Heubeck, 2001; Metcalfe, 2013, 2006; Wang et al., 2024; Zhao et al., 2018; Li et al., 2015), or Qaidam may have been independent from both suture (Cao et al., 2017; Wang et al., 2016).

We collected paleomagnetic data from Middle Triassic volcanic rocks of the Elashan Formation and coeval intrusive rocks in the southern Shiguigou section in the northeast of the

Qaidam Block. We will compare our new pole with well-defined apparent polar wander paths from the North China Block and Eurasia, and with previous data from Qaidam Block and estimate post-Middle Triassic convergence with Eurasia or North China. We will discuss our results in the context of locating the cryptic final Mesozoic intra-Asian plate boundary during the final amalgamation of the Eurasian continent.

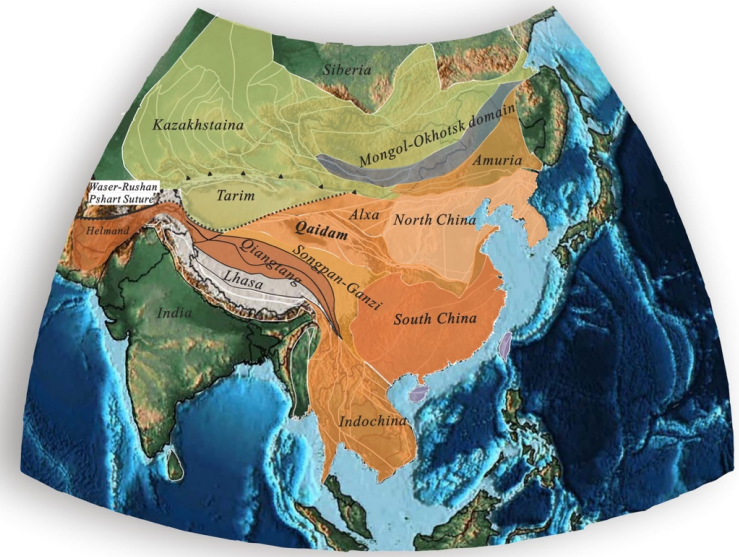

Figure 1. Tectonic map of eastern Eurasia (modified after Huang et al., 2018; Van Hinsbergen et al., 2011).

2 Geological Setting and Sampling

The Qaidam Block constitutes continental crust that underlies the Qaidam Basin of the northern Tibetan Plateau, and whose Paleozoic stratigraphy is exposed in surrounding fold-thrust belts. The block was intruded by the Kunlun Arc in Carboniferous to Triassic time that formed during subduction of the Paleo-Tethyan oceanic lithosphere to the south (Chen et al., 2015; Ding et al., 2014; Dong et al., 2018, 2020; Fan et al., 2022; Zhu et al., 2022). The Elashan Formation, target of our study, formed in the final, Middle to Late Triassic stages of this arc magmatism and is dominated by pyroclastic rocks, with intercalated lavas and clastic sedimentary rocks (Ding et al., 2014; Liu et al., 2015; Lu et al., 2012).

Our study area is in the southern and northern parts of the Qaidam Block. The Elashan formation is widely exposed near the Dulan-Xiangride Basin (Ding et al., 2011). The formation consists of volcanic rocks, with basaltic lavas in the lower part and that become more felsic (rhyolites, ashes) at the top, interbedded with sedimentary clastic rocks. We collected dacite tuff rocks from 6 sites (59 samples) in the west of Dulan County (See Figure S1 a-e in Supporting Information). The Hacipushan Section (36.27°N,98.64°E) contains effusive volcanic rocks. The area is faulted (Chai et al., 2024), and we collected samples away from these faults. In addition,

we collected the Triassic intrusive rocks (39 samples from 6 sites; 36.27°N, 98.64°E) from the Shihuigou section, which are approximately 251 Ma (Sun et al., 2022). The lithology is mainly fine-grained rhyolitic hypabyssal rocks that intrude the Proterozoic. These rocks occur predominantly as sills, showing a concordant intrusive relationship with the host Proterozoic strata (Wang et al., 2022a). The intrusive sills share the same bedding attitude as the host strata.

All the samples were collected by a portable gasoline-powered drill and were oriented by both magnetic and solar compass (Figures 2a and 2b). The discrepancy in declination between these two orienting techniques is insignificant, implying that any local magnetic disturbance can be considered negligible. At the same time, we have collected 2 samples from the Hacipushan and Shihuigou sections for the zircon U-Pb geochronological.

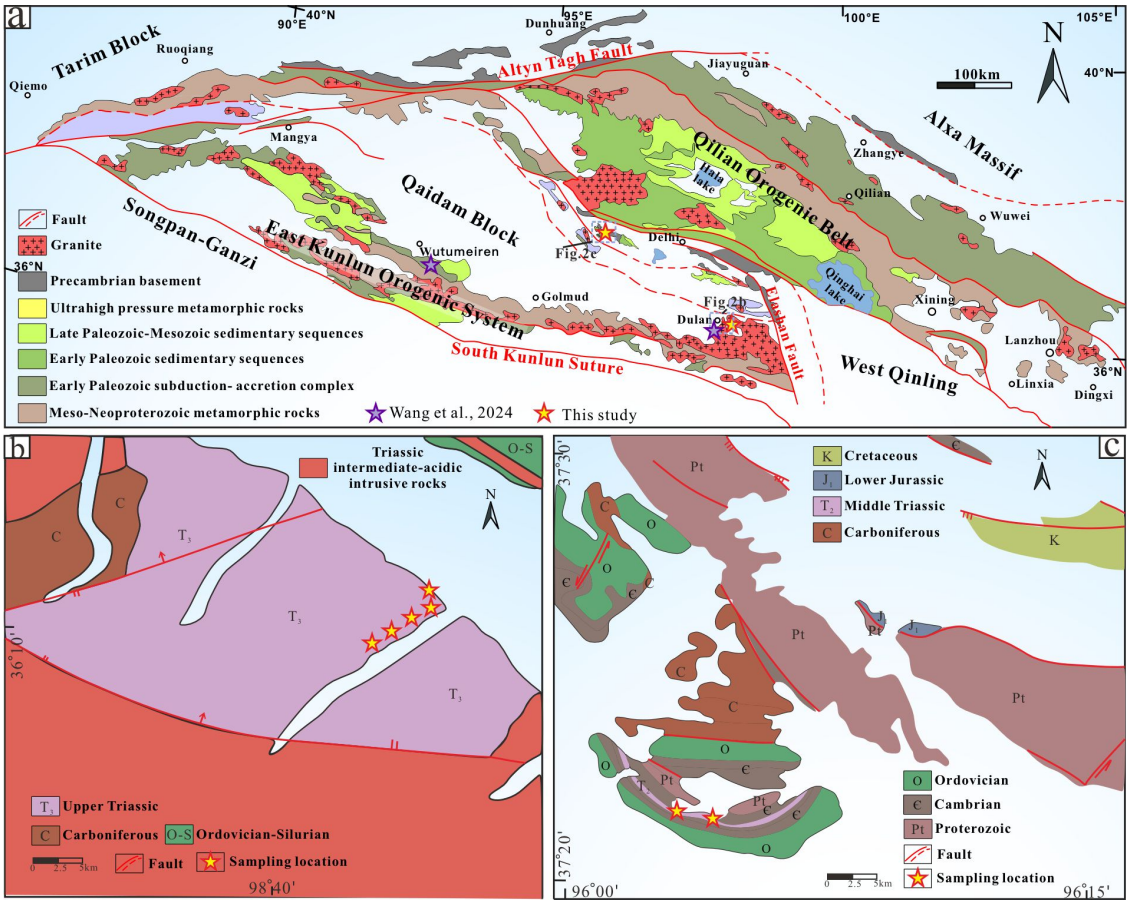

Figure 2. Geologic map of the study area showing structural relationships and the distribution of paleomagnetic sampling sections. (a) Schematic geological map of the QB and its surrounding blocks (modified from Wang et al., 2022c). (b) Geological map of the sampling locations in the Dulan area (QBGMR, 1976). (c) Geological map of the sampling locations in the Shihuigou area (QBGMR, 1976).

3 Results

3.1 Zircon U-Pb Age

Zircons of the sample from the Hacipushan section show well-developed euhedral prismatic shape and oscillatory growth zoning (Figure 3a). Forty zircons were analyzed, and after rejection of discordant, 37 age points yield 207Pb/235U age at 235.6 ± 1.6 Ma (MSWD = 0.65), which we use to approximate the extrusion age for this volcanic sequence (Figure 3c,d).

The 32 zircons were analysed on the sample from the Shihuigou section yielded reliable 28 ages with concordance between 90% and 110%. About 84% of these zircons exhibit Th/U values > 0.1 and magmatic internal zonings, suggesting that these zircons were primarily derived from igneous protoliths (Belousova et al., 2002; Corfu et al., 2003)(Figure 3b, e-f). Meanwhile, a significant amount of metamorphism can be observed in the CL results. Age patterns of this sample from the Shihuigou section are similar to the Quanji section in age span and main peaks (Sun et al.,2022) (Figure 3g, and h). Thus, we think that this section is deep intrusive rocks formed during the middle Triassic.

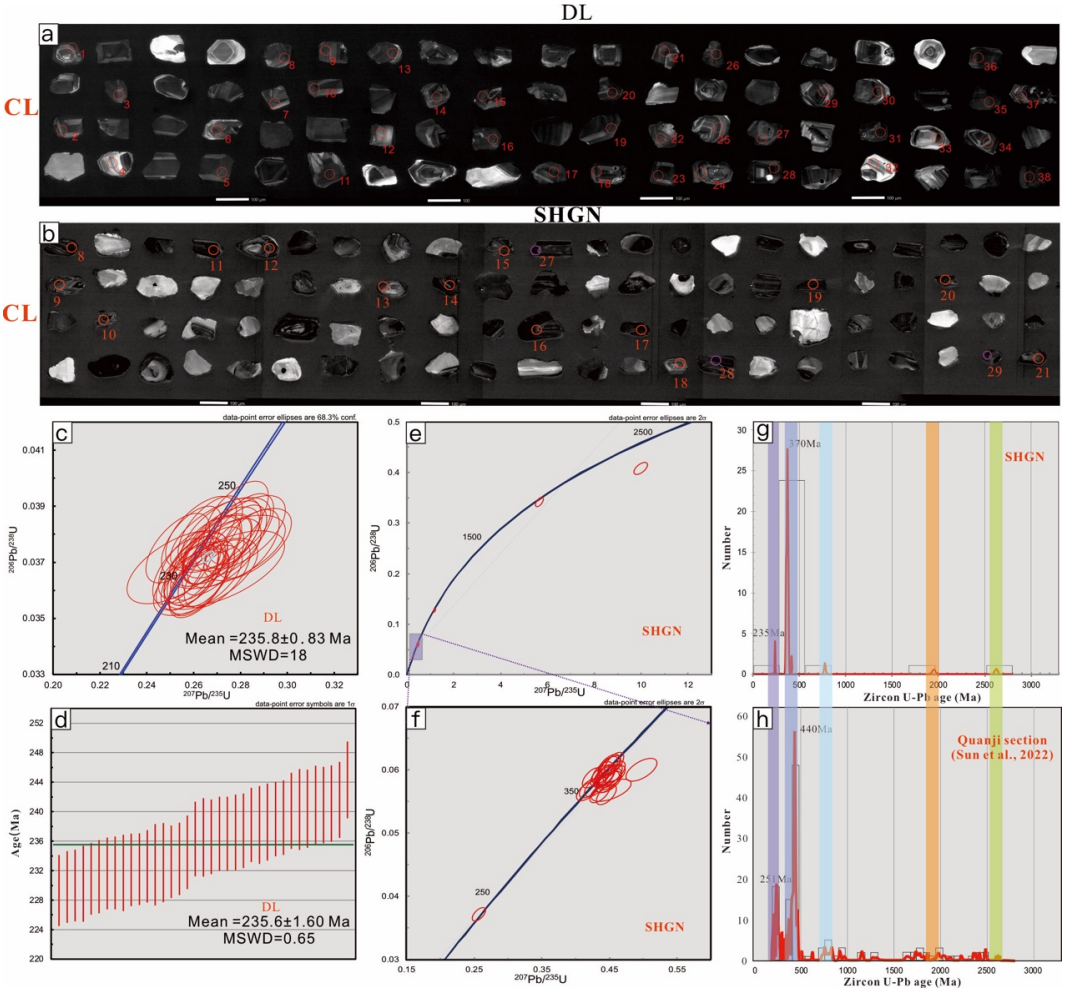

Figure 3. (a-b). Cathodoluminescence images of representative zircon grains. (c-f). Corresponding 206Pb/238U ages of the individual analyzed spots. (c-d). The result of 206Pb/238U

ages in the Dulan section. (e-f). The result of 206Pb/238U ages in the Shihuigou section. (g) Detrital zircon age distributions of representative age span and main peaks. (h) The data source was from (Sun et al., 2022).

3.2 Rock Magnetic and Paleomagnetic results

Detailed rock-magnetic experimental results are presented in the Supplementary Text in Supporting Information. The results show that most samples reach IRM saturation at ~300 mT and have remanence coercivities of ~50–100 mT, indicating the dominance of low-coercivity magnetic minerals, whereas a minor high-coercivity component is also present; combined with previous rock magnetic studies (Chai et al., 2024), this suggests that magnetite is the main magnetic carrier.

All paleomagnetic specimens were subjected to stepwise thermal demagnetization and yielded stable magnetic signals that we interpreted and analyzed using the Paleomagnetism.org online toolbox (Koymans et al., 2016; 2020). All data are provided in the supplementary information and in databases (see data availability statement). Six sites from the Hacipushan section were analyzed in detail through progressive thermal demagnetization. The remanent magnetization intensity shows a generally smooth and gradual decay during heating and is completely unblocked at approximately 580°C, suggesting that magnetite is the dominant magnetic carrier. Demagnetization behavior in the Hacipushan section is characterized by two distinct components: a low-temperature component (LTC) and a high-temperature component (HTC). The HTC began to unblock at ~500°C and is mainly isolated between 500 and 580°C, indicating a stable primary remanence (Figure 4A). Progressive thermal demagnetization experiments were also conducted on six sites from the Shihuigou section. In these samples, the LTC is largely removed by NRM–250°C, with minor inflection points appearing near 300°C (Figure 4A). During further heating, the remanent magnetization decreases steadily and is fully unblocked between ~460 and 580°C. Like the Hacipushan section, the high-temperature component from the Shihuigou section is interpreted as the characteristic remanent magnetization.

The directions of the LTC from both sections are similar, and a mean calculated from 113 samples is Dg = 5.2°±5.0°, Ig = 58.1°±3.6°, Kg = 12.7, A95g = 3.9° in geographic coordinates. The in situ LTC, removed below 500 °C, is close to the present geomagnetic field (D = 0°, I = ~57°) and is therefore interpreted as a viscous remanent magnetization acquired under the influence of the recent field (Figure 4B-a). Stepwise tectonic correction of the LTC (Tauxe and Watson, 1994) yields an optimal clustering at 10.5 ± 6.5% unfolding, confirming that this is a post-folding overprint (Figure 4B-d).

Of the six sites from the Hacipushan section, 40 samples yielded stable directions interpreted as the Characteristic Remanent Magnetization (ChRM). Of the six sites from the Shihuigou section, 28 samples yielded stable directions. The directions from these samples, which represent 12 individual sampling sites, were averaged per site to obtain a site-mean direction. Wang et al. (2024) reported paleomagnetic data of volcanic rocks in the middle Triassic of the Qaidam Basin with similar age and sampling location to our study. We combined their and our results to arrive at an overall mean direction of Dg = 63.7°±9.9°, Ig = 47.0°±10.4°, A95g=8.7°,

Kg=7.7 before tilt correction, and Ds=43.3°±4.9°, Is=54.2°±4.1°, A95s=4.1°, Ks=32.1 after tilt correction (Figure 4B-b and c, Table S3 in Supporting Information). We perform the Tauxe and Watson (1994) fold test, which yields the highest τ1 value between 82% and 102%, indicating a positive fold test (Figure 4B-e). The recent bootstrap reversal test of Heslop et al (2023) is positive indicating antipodal normal and reversed directions (CTMD value=14.59; CTMD critical value=18.43; CMDT p-value=0.09). Finally, the A95, value of the 40 VGPs (4.1), which falls into the N-dependent A95min, max envelope of Deenen et al. (2011) (2.74, 8.03), suggesting that the data scatter may be straightforwardly explained by paleosecular variation alone. Collectively, these results suggest that the ChRM likely represents a primary magnetization, and we compute a mean paleomagnetic pole at 54.95°N/178.18°E (Figure 4B-f; Table S3 in Supporting Information).

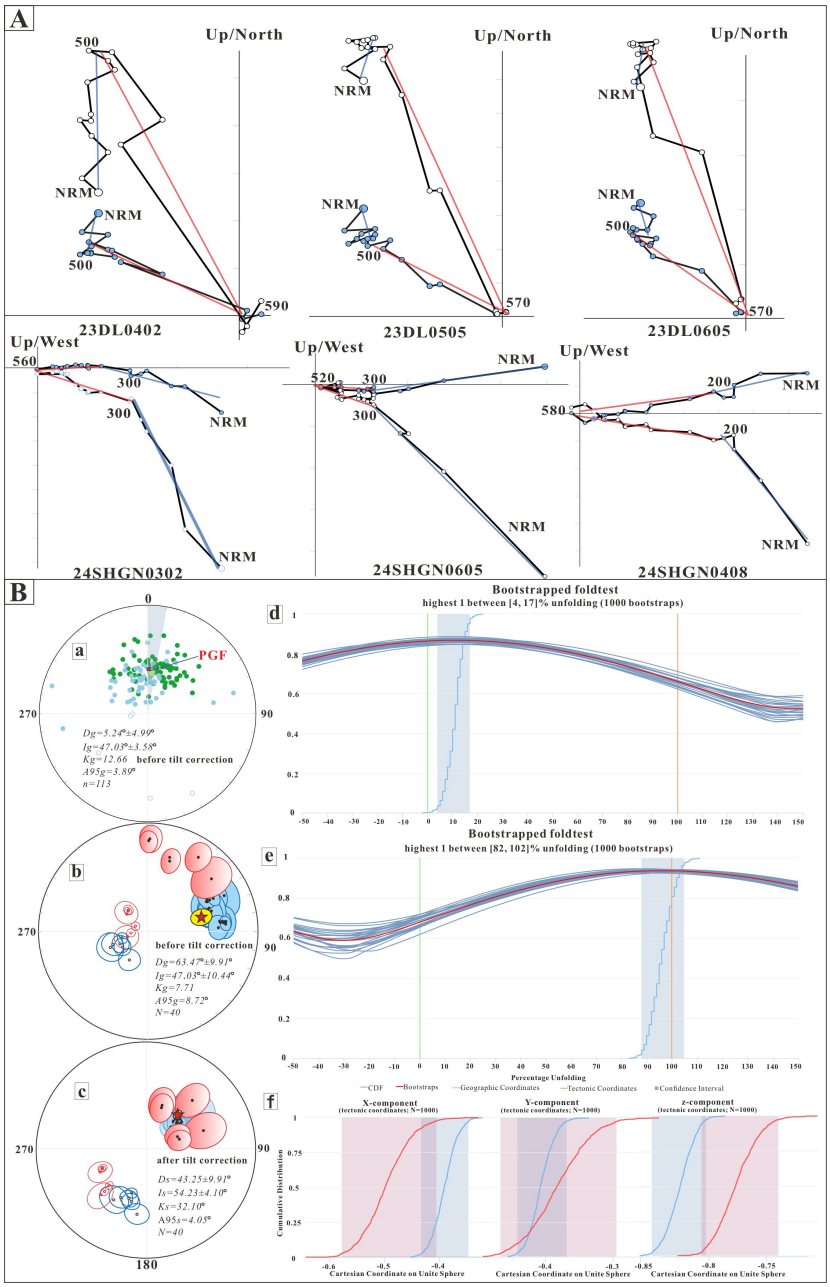

Figure 4. A. Representative demagnetization results of samples from the Hacipushan section and Shihuigou section (shown in geographic coordinates). The colored circles and colored straight lines represent the points involved in the PCA and the fitted direction, respectively. Blue (red) corresponds to the low-temperature components (high-temperature components). B. (a). Equal-area plots of the low temperature components before tilt correction. Blue-the Hacipushan section, Green-the Shihuigou section. PGF present-day geomagnetic field direction; (b)- (c). Equal-area plots of the high-temperature components in the mean sites before and after tilt correction, the mean direction calculated by using the sites from Wang et al. (2024) (in blue) and this study (in red; open circles from the Hacipushan section; closed circles from the Shihuigou section). Open/closed circles are projections on the upper/ lower hemisphere. D-declination; I-inclination; K-best estimate of the precision parameter; α95-radius of the mean direction at the 95% confidence level; n-number of samples used in mean calculation; N-number of sites used in mean calculation. (d)- (e) Results of the bootstrapped fold test in low (high)-temperature components of the samples from the Hacipushan and Shihuigou sections. (f) Bootstrap reversal test of Tauxe (2010) that reveals a negative test of our result.

4 Discussion

To interpret the paleoposition of the Qaidam Block during the middle Triassic, we first integrate our new paleomagnetic observations with previous results. We compiled poles from volcanic or inclination-shallowing corrected sedimentary rocks with scatters that represent PSV. In addition, we compiled poles that pass these criteria from the North China and the Alxa and Amuria blocks for this time interval (Figure 5a; see Figure 1 for block locations).

We used the online tool APWP-Online.org (Vaes et al., 2024) to compute a Permian to Triassic reference APWP for North China. This tool computes the APWP by bootstrapping a collection of pseudo-VGPs based on the number of directions used to compute each published pole and assigns each pseudo-VGP an age within the reported uncertainty. This way, positional and age uncertainty of the published poles is propagated (Vaes et al., 2022). The apparent polar wander path for the North China Block, spanning ages from 290 to 170 Ma, is determined by 10 paleomagnetic datasets (Figure 5a; Table S4 in Supporting Information). The paleolatitudes of the Qaidam Block from the Late Permian and Middle Triassic, including our new pole, plot on the predicted paleolatitude curve of the North China Block. This shows that the Qaidam Basin moved in unison with North China, and that the Cenozoic shortening documented in the Qilian Shan-Nan Shan belt (Zuza et al., 2016) falls within paleomagnetic uncertainty.

The Global APWP of Vaes et al (2023) in Eurasian coordinates predicts a paleolatitude for our reference location that for the Permian to Triassic is systematically ~2000 km farther north than that of North China and the Qaidam Block (Figure 5a). This shows that there was ~2000 km of post-Triassic convergence between the continent that included North China, Amuria and Qaidam and the rest of Eurasia. This convergence is well-known and has since long been ascribed to the closure of the Mongol-Okhotsk Ocean until final collision in the Early Cretaceous (Huang et al., 2018; Van der Voo et al., 2015; Wu et al., 2017; Zhao et al., 2025). However, our Triassic paleolatitude, as well as the Permian paleolatitudes (e.g., Wang et al., 2025; Song et al., 2026) demonstrate that similar convergence must have occurred between Qaidam and Tarim.

Theoretically, this motion could have been accommodated along a transform margin, but that would cause overlap of the Asian blocks with the Cimmerian blocks of Iran and even the Mediterranean region. If this convergence was accommodated by intra-continental shortening, it would be even more surprising that there is no geological record, for continental shortening leads to major fold-thrust belts - for comparison, the modern Tien Shan mountains resulted from less than 200 km of shortening (Avouac et al., 1993; Yin et al., 1998). We see no alternative than to hypothesize, similar to Wang et al. (2025), that an ocean basin, connected northeastwards to the Mongol-Okhotsk Ocean, separated Qaidam and Tarim in Triassic time (Figure 5b).

It is of course surprising that a suture of the relatively young age and magnitude is not directly evident in geological records. In part, this may be explained if the suture and associated arc rocks are buried below younger sedimentary cover of the Tarim Basin (Wang et al., 2025). Alternatively, or additionally, part may have been burried below the northwestern Tibetan Plateau by transpression along the Altyn Tagh Fault or its precursors. The most promising locations to identify this suture may be by mapping the western termination of the Solonker Suture, which must abut against the cryptic suture. In addition, it has been hypothesized that restoring back-arc basin sutures in Iran would shift the Helmand Block of Afghanistan eastward, potentially linking it to the western part of the Qiangtang Block of Tibet. The Helmand Block is bounded to the north by the early Cretaceous Waser Suture (Montenat, 2009), and such a young age was also reported from the eastern continuation of this suture in the Pamir region (Rushan Pshart, Yogibekov et al., 2023). The Qiangtang terrane that had already in Triassic time sutured with the Qaidam Block as shown by the age of the intervening Songpang-Ganzi accretionary complex that marks the remains of the Paleotethys Ocean (Dong et al., 2018; Yin and Harrison, 2000). The Waser Suture shows that the Helmand-Qiangtang Block was in the northwest bounded by an oceanic subduction zone from Eurasia, and that this subduction zone ceased at the same time as the closure of the Mongol-Okhotsk Ocean. This is consistent with the Paleomagnetic data that we show here for the Qaidam Block and may form another starting point to carefully map out the youngest intra-Asian plate boundary that preceded final Eurasian assembly.

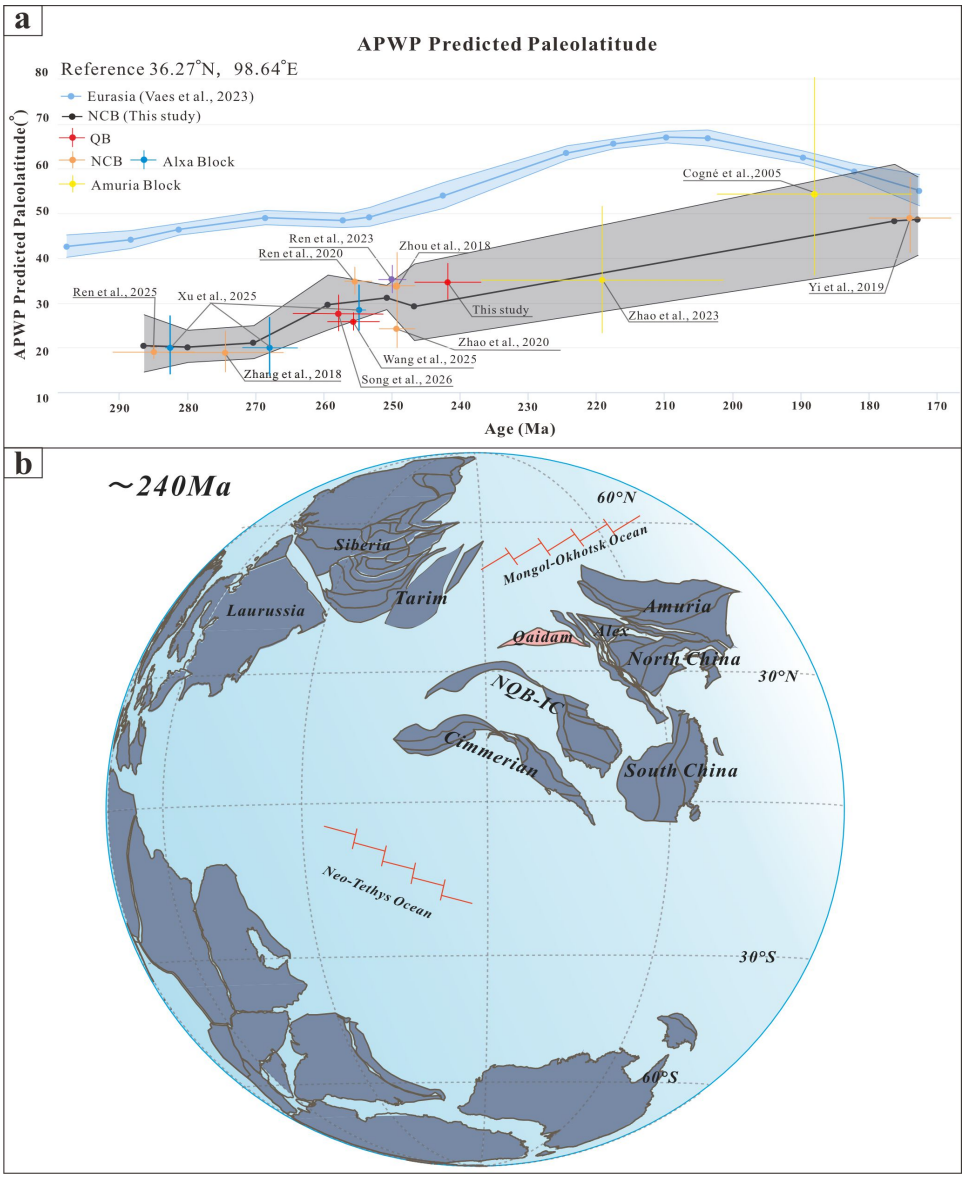

Figure 5. (a) Paleolatitudinal comparison with Eurasia, North China (and its surrounding blocks), Qaidam, and North Qiangtang Blocks during the Permian-Triassic. The paleolatitude evolution was calculated and drawn using the online tools APWP-Online.org (Vaes et al., 2024) and paleomagnetism.org (Koymans et al., 2016, 2020), respectively. Paleolatitudes are calculated with a reference point at 36.27°N/98.64°E. Data compilation based on (Cogné et al., 2005,Ren et al., 2025, 2020; Song et al., 2026; Wang et al., 2024, 2025; Xu et al., 2025; Yi et al., 2019; Zhang et al., 2018; Zhao et al., 2023, 2020; Zhou et al., 2018) (see Supplementary Table S4). (b) Schematic paleogeographic reconstruction of the East Asian blocks, Laurussia and Siberia. The QB is positioned according to the data in this study. Amuria, South China, Cimmeria, the Tethyan oceans, and the major continents follow reconstructions of (Huang et al., 2018; Ren et al., 2020; Van Hinsbergen et al., 2020; Wang et al., 2025; Xu et al., 2025). North Qingtang-Indo-china (NQB-IC) and Cimmerian follow reconstructions of (Cheng et al., 2023; Guan et al., 2021; Wei et al., 2022). and placed in the paleomagnetic reference frame of (Vaes et al., 2023).

5 Conclusions

New paleomagnetic and geochronological data from Middle-Late Triassic volcanic and intrusive rocks of the QB provide robust constraints on its paleoposition and kinematic evolution from the Middle to Late Triassic. Primary paleomagnetic results yield a ~240 Ma paleolatitude of ~35°N for the QB, statistically indistinguishable from that of the North China Block, indicating that the two blocks had entered a common convergent tectonic framework by at least the Middle Triassic. In contrast, comparison with the Eurasian apparent polar wander path reveals a persistent paleolatitudinal offset exceeding ~2000 km, requiring the presence of a cryptic oceanic domain west of the North China–Qaidam assemblage during the Early–Middle Triassic. Furthermore, our data provide additional support for the hypothesis that the Mongol–Okhotsk suture extends southwestward and connects with the Waser suture in Afghanistan. Accordingly, we infer that a cryptic (and possibly buried) suture zone is likely present below the Tarim Basin, or below the NW Tibetan Plateau, which marks the last plate boundary that culminated in the assembly of Eurasia.

Acknowledgments

This work was supported by the National Natural Science Foundation of China (42372251 and 42274097).

Conflict of Interest

The authors declare no conflicts of interest relevant to this study.

Data Availability Statement

All data supporting the findings of this study are available in the supporting information for peer review and will be deposited in the Zenodo repository upon acceptance of the manuscript.

References

Avouac, J. P., Tapponnier, P., Bai, M., You, H., & Wang, G. (1993). Active thrusting and folding along the northern Tien Shan and Late Cenozoic rotation of the Tarim relative to Dzungaria and Kazakhstan. *Journal of Geophysical Research: Solid Earth*, 98(B4), 6755–6804. https://doi.org/10.1029/92JB01963

Belousova, E., Griffin, W., O'Reilly, S. Y., & Fisher, N. (2002). Igneous zircon: trace element composition as an indicator of source rock type. *Contributions to Mineralogy and Petrology*, 143(5), 602–622. https://doi.org/10.1007/s00410-002-0364-7

Bu, J.J., He, W.H., Zhang, K.X., Yu, Y., Wang, J.X., & Wu, J. (2020). Evolution of the Paleo-Asian Ocean: Evidences from Paleontology and Stratigraphy. *Earth Science-Journal of China University of Geosciences*, 45(3), 711 (in Chinese).

Cao, Y., Sun, Z.M., Li, H.B., Pei, J.L., Xu, W., Pan, J.W., et al. (2017). New Early and Late Carboniferous paleomagnetic results from the Qaidam Block, NW China: Implications for the paleogeography of Central Asia. *Tectonophysics*, 717, 242–252. https://doi.org/10.1016/j.tecto.2017.08.014

Chai, R.Y., Zhou, Y.N., Wang, T., Cheng, X., Wei, B.T., Jiang, N., et al. (2024). New Rock Magnetism and Magnetic Fabrics Studies on the Late Triassic Volcanic Rocks from Qaidam Block, Northern Tibetan Plateau. *Minerals*, 14(5), 515. https://doi.org/10.3390/min14050515

Chen, J., Wang, B.Z., Li, B., Zhang, Z.Q., Qiao, B.X., & Jin, T.T. (2015). Zircon U–Pb ages, geochemistry, and Sr–Nd–Pb isotopic compositions of Middle Triassic granodiorites from the Kaimuqi area, East Kunlun, Northwest China: implications for slab breakoff. *International Geology Review*, 57(2), 257–270. https://doi.org/10.1080/00206814.2014.1003105

Cheng, X., Wei, B.T., Jiang, N., Zhou, Y.N., Kravchinsky, V. A., Chen, Q.L., et al. (2023). Evolution of the North Qiangtang Block in the late Paleozoic: Paleomagnetism and its tectonic implications. *Geological Society of America Bulletin*, 136 (1-2): 707–724. https://doi.org/10.1130/B36825.1

Cogné, J.-P., Kravchinsky, V. A., Halim, N., & Hankard, F. (2005). Late Jurassic-Early Cretaceous closure of the Mongol-Okhotsk Ocean demonstrated by new Mesozoic palaeomagnetic results from the Trans-Baïkal area (SE Siberia). Geophysical Journal International, 163(2), 813–832. https://doi.org/10.1111/j.1365-246X.2005.02782.x

Cocks, L. R. M., & Torsvik, T. H. (2013). The dynamic evolution of the Palaeozoic geography of eastern Asia. *Earth Science Reviews*, 117, 40–79. https://doi.org/10.1016/j.earscirev.2012.12.001

Corfu, F., Hanchar, J. M., Hoskin, P. W., & Kinny, P. (2003). Atlas of zircon textures. *Reviews in mineralogy and geochemistry*, 53(1), 469-500. https://doi.org/10.2113/0530469

Deenen, M. H. L., Langereis, C. G., Van Hinsbergen, D. J. J., & Biggin, A. J. (2011). Geomagnetic secular variation and the statistics of palaeomagnetic directions: Statistics of palaeomagnetic directions. Geophysical Journal International, 186(2), 509–520. https://doi.org/10.1111/j.1365-246X.2011.05050.x

Ding, S., Huang, H., Niu, Y.L., Zhao, Z.D., Yu, X.H., & Mo, X.X. (2011). Geochemistry, geochronology and petrogenesis of East Kunlun high Nb-Ta rhyolites. *Acta Petrologica Sinica*, 27(12), 3603–3614 *(in Chinese)*.

Ding, Q.F., Jiang, S.Y., & Sun, F.Y. (2014). Zircon U–Pb geochronology, geochemical and Sr–Nd–Hf isotopic compositions of the Triassic granite and diorite dikes from the Wulonggou mining area in the Eastern Kunlun Orogen, NW China: Petrogenesis and tectonic implications. *Lithos*, 205, 266–283. https://doi.org/10.1016/j.lithos.2014.07.015

Dong, J.L., Song, S.S., Su, L., Allen, M. B., Li, Y.G., & Wang, C. (2020). Early Devonian mafic igneous rocks in the East Kunlun Orogen, NW China: Implications for the transition from the Proto- to Paleo-Tethys oceans. *Lithos*, 376–377, 105771. https://doi.org/10.1016/j.lithos.2020.105771

Dong, Y. P., Sun, S.S., Santosh, M., Zhao, J., Sun, J.P., He, D.F., et al. (2021). Central China Orogenic Belt and amalgamation of East Asian continents. *Gondwana Research*, 100, 131–194. https://doi.org/10.1016/j.gr.2021.03.006

Dong, Y.P., He, D.F., Sun, S.S., Liu, X.M., Zhou, X.H., Zhang, F.F., et al. (2018). Subduction and accretionary tectonics of the East Kunlun orogen, western segment of the Central China Orogenic System. *Earth Science Reviews*, 186, 231–261. https://doi.org/10.1016/j.earscirev.2017.12.006

Eizenhöfer, P. R., & Zhao, G.C. (2018). Solonker Suture in East Asia and its bearing on the final closure of the eastern segment of the Palaeo-Asian Ocean. *Earth Science Reviews*, 186, 153–172. https://doi.org/10.1016/j.earscirev.2017.09.010

Fan, X.Z., Sun, F.Y., Xu, C.H., Wu, D.Q., Yu, L., Wang, L., et al. (2022). Volcanic rocks of the Elashan Formation in the Dulan-Xiangride Basin, East Kunlun Orogenic Belt, NW China: Petrogenesis and implications for Late Triassic geodynamic evolution. *International Geology Review*, 64(9), 1270–1293. https://doi.org/10.1080/00206814.2021.1923074

Guan, C., Yan, M.D., Zhang, W.L., Zhang, D.W., Fu, Q., Yu, L., et al. (2021). Paleomagnetic and Chronologic Data Bearing on the Permian/Triassic Boundary Position of Qamdo in the Eastern Qiantang Terrane: Implications for the Closure of the Paleo-Tethys. *Geophysical Research Letters*, 48(6), e2020GL092059. https://doi.org/10.1029/2020GL092059

Heslop, D., Scealy, J. L., Wood, A. T. A., Tauxe, L., & Roberts, A. P. (2023). A Bootstrap Common Mean Direction Test. Journal of Geophysical Research: Solid Earth, 128(8), e2023JB026983. https://doi.org/10.1029/2023JB026983

Heubeck, C. (2001). Assembly of central Asia during the middle and late Paleozoic, in Paleozoic and Mesozoic Tectonic Evolution of Central and Eastern Asia. *Geological Society of America*, 194, 1–22,. https://doi.org/10.1130/0-8137-1194-0.1

Huang, B.C., Yan, Y.G., Piper, J. D. A., Zhang, D.H., Yi, Z.Y., Yu, S., & Zhou, T.H. (2018). Paleomagnetic constraints on the paleogeography of the East Asian blocks during Late Paleozoic and Early Mesozoic times. *Earth Science Reviews*, 186, 8–36. https://doi.org/10.1016/j.earscirev.2018.02.004

Jolivet, M., Arzhannikova, A., Frolov, A., Arzhannikov, S., Kulagina, N., Akulova, V., & Vassallo, R. (2017). Late Jurassic - Early Cretaceous paleoenvironmental evolution of the Transbaikal basins (SE Siberia): implications for the Mongol-Okhotsk orogeny. *Bulletin de La Société Géologique de France*, 188(1–2), 9. https://doi.org/10.1051/bsgf/2017010

Koymans, M.R., Langereis, C.G., Pastor-Galán, D., & van Hinsbergen, D.J.J. (2016). Paleomagnetism.org: An online multi-platform open source environment for paleomagnetic data analysis. *Computers & Geosciences*, 93, 127-137, https://doi.org/10.1016/j.cageo.2016.05.007.

Koymans, M.R., van Hinsbergen, D.J.J., Pastor-Galan, D., Vaes, B. and Langereis, C.G. (2020). Towards FAIR paleomagnetic data management through Paleomagnetism. org 2.0. *Geochemistry, Geophysics, Geosystems*, e2019GC008838. https://doi.org/10.1029/2019GC008838

Li, J.H., Zhou, X.B., Li, W.B., Wang, H.H., Liu, Z.L., Zhang, H.T., & Abitkazy, T. (2015). Preliminary Reconstruction of Tectonic Paleogeography of Tarim Basin and Its Adjacent Aeras from Cambrian to Triassic, NW China. *Geological Review*, 61(6), 1225–1234 (in Chinese).

Liu, Z., Jiang, Y.H., Jia, R.Y., Zhao, P., & Zhou, Q. (2015). Origin of Late Triassic high-K calc-alkaline granitoids and their potassic microgranular enclaves from the western Tibet Plateau, northwest China: Implications for Paleo-Tethys evolution. Gondwana Research, 27(1), 326–341. https://doi.org/10.1016/j.gr.2013.09.022

Lu, W.Q., Tong, H.K., Cang, S., & Ma, Y.S. (2012). Analysis of environment for Late Triassic volcanic rocks in Chachaxiangka, Elashan. *Northwestern Geology*, 45(1), 48–55 (in Chinese).

Metcalfe, I. (2006). Palaeozoic and Mesozoic tectonic evolution and palaeogeography of East Asian crustal fragments: The Korean Peninsula in context. *Gondwana Research*, 9(1–2), 24–46. https://doi.org/10.1016/j.gr.2005.04.002

Metcalfe, I. (2013). Gondwana dispersion and Asian accretion: Tectonic and palaeogeographic evolution of eastern Tethys. Journal of Asian Earth Sciences, 66, 1–33. https://doi.org/10.1016/j.jseaes.2012.12.020

Metcalfe, Ian. (2021). Multiple Tethyan ocean basins and orogenic belts in Asia. *Gondwana Research*, 100, 87–130. https://doi.org/10.1016/j.gr.2021.01.012

Montenat, C. 2009. The mesozoic of Afghanistan. *GeoArabia*, 14, 147-210. https://doi.org/10.2113/geoarabia1401147

QBGMR (Qinghai Bureau of Geology and Mineral Resources). (1976). Regional geological investigation of the Dulan Area, Beijing: Regional geology of Qinghai Province supply paper (in Chinese).

Ren, Q., Zhang, S.H., Gao, Y.J., Zhao, H.Q., Wu, H.C., Yang, T.S., & Li, H.Y. (2020). New Middle–Late Permian Paleomagnetic and Geochronological Results From Inner Mongolia and their Paleogeographic Implications.

Journal of Geophysical Research: Solid Earth, 125(7), e2019JB019114. https://doi.org/10.1029/2019JB019114

Ren, Q., Zhang, S.H., Hou, M.C., Zheng, D.Y., Wu, H.C., Yang, T.S., et al. (2025). Continental drift triggered the Early Permian aridification of North China. *Nature Communications*, 16(1), 384. https://doi.org/10.1038/s41467-024-55804-8

Sharps, R., McWilliams, M., Li, Y.P., Cox, A., Zhang, Z.K., Zhai, Y.J., et al. (1989). Lower Permian paleomagnetism of the Tarim block, northwestern China. *Earth and Planetary Science Letters*, 92(3–4), 275–291. https://doi.org/10.1016/0012-821X(89)90052-6

Song, P.P., Ding, L., Zhang, L., Wu, C., Duan, X.Y., Yue, Y.H., & Xie, J. (2026). Defining the main Paleo-Tethys suture in Tibet: First Permian paleomagnetic insights from the Eastern Kunlun Range. *Earth and Planetary Science Letters*, 681, 119925. https://doi.org/10.1016/j.epsl.2026.119925

Sun, J.P., & Dong, Y.P. (2020). Stratigraphy and geochronology of Permo-Carboniferous strata in the Western North China Craton: Insights into the tectonic evolution of the southern Paleo-Asian Ocean. *Gondwana Research*, 88, 201–219. https://doi.org/10.1016/j.gr.2020.08.005

Sun, Y.P., Ouyang, Q., Pang, K., Wu, C.X., Chen, Z., Yuan, X.L., & Zhou, C.M. (2022). Detrital zircon geochronology and stratigraphy of the Proterozoic strata in the Olongbuluke terrane of Northwest China: Implications for the Great Unconformity. *Precambrian Research*, 376, 106684. https://doi.org/10.1016/j.precamres.2022.106684

Tauxe, L. (2010). Essentials of Paleomagnetism, *Univ. of California Press, Berkeley*. https://doi.org/10.1525/9780520946378

Tauxe, L., & Watson, G.S. (1994). The fold test: an eigen analysis approach. *Earth and Planetary Science Letters*, 122(3–4), 331–341. https://doi.org/10.1016/0012-821X(94)90006-X

Vaes, B., Gallo, L.C., & Van Hinsbergen, D.J.J. (2022). On Pole Position: Causes of Dispersion of the Paleomagnetic Poles Behind Apparent Polar Wander Paths. *Journal of Geophysical Research: Solid Earth*, 127(4), e2022JB023953. https://doi.org/10.1029/2022JB023953

Vaes, B., Van Hinsbergen, D.J.J., Van De Lagemaat, S.H.A., Van Der Wiel, E., Lom, N., Advokaat, E. L., et al. (2023). A global apparent polar wander path for the last 320 Ma calculated from site-level paleomagnetic data. *Earth Science Reviews*, 245, 104547. https://doi.org/10.1016/j.earscirev.2023.104547

Vaes, B., van Hinsbergen, D. J., & Paridaens, J. (2024). APWP-online.org: A global reference database and open-source tools for calculating apparent polar wander paths and relative paleomagnetic displacements. *Tektonika*, 2(1), 174–189. https://doi.org/10.55575/tektonika2024.2. 1.44

Van der Voo, R., van Hinsbergen, D. J., Domeier, M., Spakman, W., & Torsvik, T. H. (2015). Latest Jurassic–earliest Cretaceous closure of the Mongol-Okhotsk Ocean: A paleomagnetic and seismological-tomographic analysis. *Geological Society of America Special Paper, 513, 589606*. https://doi.org/10.1130/2015.2513(19)

Van Hinsbergen, D.J.J., Kapp, P., Dupont-Nivet, G., Lippert, P. C., DeCelles, P. G., & Torsvik, T.H. (2011). Restoration of Cenozoic deformation in Asia and the size of Greater India. *Tectonics*, 30(5), TC5003. https://doi.org/10.1029/2011TC002908

Van Hinsbergen, D.J.J., Torsvik, T. H., Schmid, S.M., Maţenco, L.C., Maffione, M., Vissers, R.L.M., et al. (2020). Orogenic architecture of the Mediterranean region and kinematic reconstruction of its tectonic evolution since the Triassic. *Gondwana Research*, 81, 79–229. https://doi.org/10.1016/j.gr.2019.07.009

Wang, B., Huang, B.C., Yang, Z.Y., Zhang, G.W., Liu, X.M., Duan, L., et al. (2024). Palaeomagnetic results from Early Mesozoic strata in the Qaidam Basin and their implications for the formation of the Northern China Domain. *Geophysical Journal International*, 236(3), 1621–1635. https://doi.org/10.1093/gji/ggad496

Wang, B., Zhang, G.W., Li, S.Z., Yang, Z.Y., Roberts, A. P., Zhao, Q., & Wang, Z.Y. (2016). Early Carboniferous paleomagnetic results from the northeastern margin of the Qinghai–Tibetan plateau and their implications. Gondwana Research, 36, 57–64. https://doi.org/10.1016/j.gr.2016.04.007

Wang, C., Evans, D. A. D., Li, M., Zhang, J.H., Han, J., Wen, B., et al. (2022a). Proterozoic-Mesozoic development of the Quanji block from northern Tibet and the cratonic assembly of eastern Asia. American Journal of Science, 322(5), 705–727. https://doi.org/10.2475/05.2022.03

Wang, C., Evans, D.A.D., Li, M., Zhang, J.H., Zhao, J., & Wen, B. (2020). Tectono-stratigraphic framework of late

460 Paleoproterozoic to Cambrian strata of the Quánjí block and its role in the development of northern Tibet
461 Plateau orogenic collage. Geology. https://doi.org/10.1002/essoar.10505612.1
462 Wang, T., Tong, Y., Xiao, W.J., Guo, L., Windley, B. F., Donskaya, T., et al. (2022b). Rollback, scissor-like closure of
463 the Mongol-Okhotsk Ocean and formation of an orocline: magmatic migration based on a large archive of
464 age data. *National Science Review*, 9(5), nwab210. https://doi.org/10.1093/nsr/nwab210
465 Wang, T., Zhou, Y.N., Van Hinsbergen, D. J. J., Sun, J.P., Cheng, X., Chai, R.Y., et al. (2025). Paleomagnetic Evidence
466 for a Late Permian Qaidam-North China Connection, and the Cryptic Final Mesozoic Intra-Asian Suture.
467 *Journal of Geophysical Research: Solid Earth*, 130(8), e2025JB031123.
468 https://doi.org/10.1029/2025JB031123
469 Wang, T., Zhou, Y.N., He, W.D., He, L., Cheng, X., Deng, X.H., et al. (2022c). Provenance change in Carboniferous-
470 early Permian sedimentary successions in the North Qaidam tectonic belt, northern Tibetan Plateau:
471 Implications for the Kunlun oceanic plate subduction process. *Journal of Asian Earth Sciences*, 240, 105434.
472 https://doi.org/10.1016/j.jseaes.2022.105434
473 Wei, B., Yang, X.F., Cheng, X., Domeier, M., Wu, H.N., Kravchinsky, V.A., et al. (2020). An Absolute
474 Paleogeographic Positioning of the Early Permian Tarim Large Igneous Province. *Journal of Geophysical*
475 *Research: Solid Earth*, 125(5), e2019JB019111. https://doi.org/10.1029/2019JB019111
476 Wei, B.T., Cheng, X., Domeier, M., Jiang, N., Wu, Y.Y., Zhang, W.J., et al. (2022). Placing Another Piece of the
477 Tethyan Puzzle: The First Paleozoic Paleomagnetic Data From the South Qiangtang Block and Its
478 Paleogeographic Implications. *Tectonics*, 41(10), e2022TC007355. https://doi.org/10.1029/2022TC007355
479 Wu, L., Kravchinsky, V. A., & Potter, D. K. (2017). Apparent polar wander paths of the major Chinese blocks since
480 the Late Paleozoic: Toward restoring the amalgamation history of east Eurasia. *Earth Science Reviews*, 171,
481 492–519. https://doi.org/10.1016/j.earscirev.2017.06.016
482 Xiao, W.J., Song, D.F., Windley, B.F., Li, J.L., Han, C.M., Wan, B., et al. (2020). Accretionary processes and
483 metallogenesis of the Central Asian Orogenic Belt: Advances and perspectives. *Science China Earth*
484 *Sciences*, 63(3), 329–361. https://doi.org/10.1007/s11430-019-9524-6
485 Xiao, W.J., Windley, B. F., Sun, S., Li, J., Huang, B., Han, C., et al. (2015). A Tale of Amalgamation of Three Permo-
486 Triassic Collage Systems in Central Asia: Oroclines, Sutures, and Terminal Accretion. Annual Review of Earth
487 and Planetary Sciences, 43(1), 477–507. https://doi.org/10.1146/annurev-earth-060614-105254
488 Xiao, W.J., Windley, B. F., Yong, Y., Yan, Z., Yuan, C., Liu, C.Z., & Li, J.L. (2009). Early Paleozoic to Devonian multiple-
489 accretionary model for the Qilian Shan, NW China. *Journal of Asian Earth Sciences*, 35(3–4), 323–333.
490 https://doi.org/10.1016/j.jseaes.2008.10.001
491 Xiao, W.J., Windley, B.F., Allen, M. B., & Han, C.M. (2013). Paleozoic multiple accretionary and collisional
492 tectonics of the Chinese Tianshan orogenic collage. Gondwana Research, 23(4), 1316–1341.
493 https://doi.org/10.1016/j.gr.2012.01.012
494 Xu, W., Song, B., Shi, J.Z., Li, Y., Wang, B.W., Ye, X.Z., et al. (2025). New Permian Paleomagnetic and
495 Geochronologic Results From the Alxa Block: Constraints on Its Tectonic Affinity and the Closure of Paleo-
496 Asian Ocean. *Geophysical Research Letters*, 52(20), e2025GL116752.
497 https://doi.org/10.1029/2025GL116752
498 Yi, Z.Y., Liu, Y.Q., & Meert, J. G. (2019). A true polar wander trigger for the Great Jurassic East Asian Aridification.
499 *Geology*, 47(12), 1112–1116. https://doi.org/10.1130/G46641.1
500 Yin, A., & Harrison, T. M. (2000). Geologic Evolution of the Himalayan-Tibetan Orogen. *Annual Review of Earth*
501 *and Planetary Sciences*, 28(1), 211–280. https://doi.org/10.1146/annurev.earth.28.1.211
502 Yin, A., Nie, S., Craig, T. M., Harrison, T. M., Qian, X. L., Yang, G., & Geng, Y. (1998). Late Cenozoic tectonic
503 evolution of the southern Chinese Tian Shan. *Tectonics*, 17(1), 1–27. https://doi.org/10.1029/97TC03140
504 Yogibekov, D., Sang, M., Xiao, W.J., Mamadjonov, Y., Zhou, C.M., Yang, H., et al. (2023). Post-collisional
505 magmatism associated with the final closure of the Rushan-Pshart Meso-Tethys Ocean in Pamir, Tajikistan:
506 Inference from Cretaceous igneous rocks of the Pshart accretionary complex. *Frontiers in Earth Science*,
507 10, 1090952. https://doi.org/10.3389/feart.2022.1090952
508 Zhang, D.H., Huang, B.C., Zhao, J., Meert, J. G., Zhang, Y., Liang, Y.L., et al. (2018). Permian Paleogeography of
509 the Eastern CAOB: Paleomagnetic Constraints From Volcanic Rocks in Central Eastern Inner Mongolia, NE

China. *Journal of Geophysical Research: Solid Earth*, 123(4), 2559–2582. https://doi.org/10.1002/2018JB015614

Zhang, J., Zhang, B.H., & Zhao, H. (2016). Timing of amalgamation of the Alxa Block and the North China Block: Constraints based on detrital zircon U–Pb ages and sedimentologic and structural evidence. *Tectonophysics*, 668–669, 65–81. https://doi.org/10.1016/j.tecto.2015.12.006

Zhao, G.C., Wang, Y.J., Huang, B.C., Dong, Y.P., Li, S.Z., Zhang, G.W., & Yu, S. (2018). Geological reconstructions of the East Asian blocks: From the breakup of Rodinia to the assembly of Pangea. *Earth Science Reviews*, 186, 262–286. https://doi.org/10.1016/j.earscirev.2018.10.003

Zhao, P., Appel, E., & Xu, B. (2020). An Inclination Shallowing-Corrected Early Triassic Paleomagnetic Pole for the North China Craton: Implication for the Mesozoic Geography of Proto-Asia. Journal of Geophysical Research: Solid Earth, 125(10), e2020JB019489. https://doi.org/10.1029/2020JB019489

Zhao, P., Appel, E., Deng, C., & Xu, B. (2023). Bending of the Western Mongolian Blocks Initiated the Late Triassic Closure of the Mongol-Okhotsk Ocean and Formation of the Tuva-Mongol Orocline. Tectonics, 42(5), e2022TC007475. https://doi.org/10.1029/2022TC007475

Zhao, P., Hou, Y.F., Jia, Z.H., Appel, E., Deng, C.L., & Chen, Y. (2025). A Possible Late Jurassic Final Closure of the Mongol-Okhotsk Ocean in Its Eastern Segment: Constraints From New Paleomagnetic Investigations. *Journal of Geophysical Research: Solid Earth*, 130(7), e2024JB030741. https://doi.org/10.1029/2024JB030741

Zhao, X.X., Robert S.C., Zhou, Y.X., Wu, H.R., & Wang, J. (1990). New paleomagnetic results from northern China: collision and suturing with Siberia and Kazakhstan. Tectonophysics, 181(1–4), 43–81. https://doi.org/10.1016/0040-1951(90)90008-V

Zhou, T.H., Huang, B.C., Jia, S.F., Liang, Y.L., Zhang, D.H., Zhao, Q., Zhang, Y. & Yan, Y.G. (2018). Paleomagnetic inclination shallowing in lower Triassic Liujiagou Formation from Qinshui basin, *North China block, Acta Sci. Nat. Univ. Pekinensis*, 54(3), 521–534. doi:10.13209/j.0479- 8023.2017.100 *(in Chinese).*

Zhu, Y.X., Wang, L.X., Ma, C.Q., He, Z.X., Deng, X., & Tian, Y. (2022). Petrogenesis and tectonic implication of the Late Triassic A1-type alkaline volcanics from the Xiangride area, eastern segment of the East Kunlun Orogen (China). *Lithos*, 412–413, 106595. https://doi.org/10.1016/j.lithos.2022.106595

Zuza, A. V., Cheng, X., & Yin, A. (2016). Testing models of Tibetan Plateau formation with Cenozoic shortening estimates across the Qilian Shan–Nan Shan thrust belt. *Geosphere*, 12(2), 501–532. https://doi.org/10.1130/GES01254.1

Geophysical Research Letters

Supporting Information for

Paleomagnetic data from the Qaidam Block quantify post-middle Triassic convergence preceding eastern Eurasian assembly

Ruiyang Chai[1,2]; Yanan Zhou[1*]; Douwe J. J. van Hinsbergen[2]; Teng Wang[1]; Qiang Fu[2,3]; Zhenwei Chen[1]; Chunxi Qu[1]; Shuqi Lan[1]; Xin Cheng[1]; Hanning Wu[1]

[1]State Key Laboratory of Continental Evolution and Early Life, Department of Geology, Northwest University, Xi'an, China

[2]Department of Earth Sciences, Utrecht University, Utrecht, Netherlands

[3]Institute of Earth Sciences, Heidelberg University, Heidelberg, Germany

[*]Corresponding author: Yanan Zhou (zhouyanan@nwu.edu.cn)

Contents of this file

Supplementary Text

Laboratory Techniques

For detrital zircon geochronology, zircon grains were separated at the Langfang Regional Geological Survey in China. First, magnetic separation was employed, followed by the use of heavy liquids. Finally, the grains were hand-selected under a binocular microscope. The zircons were then embedded in epoxy resin blocks and polished to obtain flat surfaces. Cathodoluminescence imaging and U-Pb dating were performed at the State Key Laboratory of Continental Dynamics, Northwest University in Xi'an, China.

Isothermal remanent magnetization (IRM) acquisition experiments and reverse field demagnetization experiments were performed with an ASC IM-10-30 pulse magnetizer and the JR-6A magnetometer, respectively. The Cumulative log–Gaussian (CLG) curve model was also simulated for the IRM results (Heslop et al., 2002; Kruiver et al., 2001).

The rock magnetic experiments were carried out at the State Key Laboratory of Continental Dynamics, Northwest University (Xi'an, China). Other basic experiments on magnetic rock have been published in previous works (Chai et al., 2024). In this study, we will focus on the demagnetization experiments. Thermal demagnetization experiments were carried out in the Paleomagnetic Laboratory of Northwest University (Xi'an, China). The thermal demagnetization experiment used a TD-48 furnace. After each demagnetization step, magnetic remanence measurements were made with the JR-6A magnetometer and the 2G-755R low-temperature superconducting magnetometer. The samples from the Hacipushan Section exhibit higher NRM intensity, as measured by the JR-6A magnetometer. The other samples from the south of the Shihuigou section were measured by the 2G-755R low-temperature superconducting magnetometer because of the lower NRM intensity.

The analysis method of IRM curves was used with the online tool (https://shinyapps.carleton.edu/max-unmix/), which can be used to solve the unmixing problem and estimate the magnetic contribution of each component (Egli, 2003). The Paleomagnetic data analysis was conducted using the online portal Paleomagnetism.org (Koymans et al., 2020, 2016). The demagnetization results were performed on the orthogonal vector diagram (Zijderveld, 1967) and principal component analysis (Kirschvink, 1980) to determine the magnetic components. Site mean paleomagnetic directions were calculated using standard Fisher statistics (Fisher, 1953) on virtual paleomagnetic poles. All paleomagnetic data were recalculated to a common reference site (36.27°N/98.64°E) for paleolatitudinal comparison and further discussion on tectonic implications.

Rock magnetic experiments of representative samples

Rock Magnetic Results

Rock magnetic experiments were designed to identify the magnetic minerals within the rocks. In this study, we select representative samples from the Shihuigou and Hacipushan sections. The IRM curves from the Shihuigou section show two different types of magnetic minerals: (1) The IRM curve increase gradually with the increase of the magnetic field and reaches saturation at 300 mT (Figure S2, a-c); (2) The IRM curve increase gradually with the increase of the magnetic field and do not reach saturation at 2.5 T (Figure S2, d-f). The CLG model presented that there were two different magnetic minerals in the Shihuigou section samples. According to the coercivity spectrum, the results of the lower coercivity component (component 1; <80 mT), and the high coercivity component (Component 2; >3.3 T) were obtained to analyze the information of carrying magnetic minerals. Component 1 contributes up to ~94.3% of the whole SIRM in SHGN01 and ~40.8% in SHGN02. Component 1 contributes up to ~5.7% of the whole SIRM in SHGN01 and ~59.2% in SHGN02. The curves of the backfield demagnetization of saturation IRM (SIRM) in SHG01 show a maximum remanence coercive force of ~80-100 mT (Figure S2, a), indicative of the dominance of low-coercivity magnetic minerals in the samples. Whereas the curves of the backfield demagnetization of SIRM in SHG02 show a maximum remanence coercive force of ~450-500 mT (Figure S2, d), indicative of the dominance of high-coercivity magnetic minerals in the samples. Therefore, we believe that the Shihuigou section contains varying degrees of highly coercive magnetic minerals (Much greater than the coercivity of hematite, possibly goethite) and low-coercive magnetic minerals (most samples were unblocked at ~580°C, possibly magnetite).

The Hacipushan section also has two different components: Component 1 contributes up to ~91.1% of the whole SIRM in DL01, and Component 2 contributes up to ~8.9%. The curves of the backfield demagnetization of saturation IRM (SIRM) in DL01 show a maximum remanence coercive force of ~50-70 mT (Figure S2, g), indicative of the dominance of low-coercivity magnetic minerals in the samples. Combined with previous works on the rock magnetic study, we suggest that the magnetite is the main magnetic mineral carrier, with a small amount of goethite, pyrrhotite, and hematite (Chai et al., 2024). These results demonstrate that the magnetite is the dominant magnetic carrier for the primary signal.

Supplementary Figures

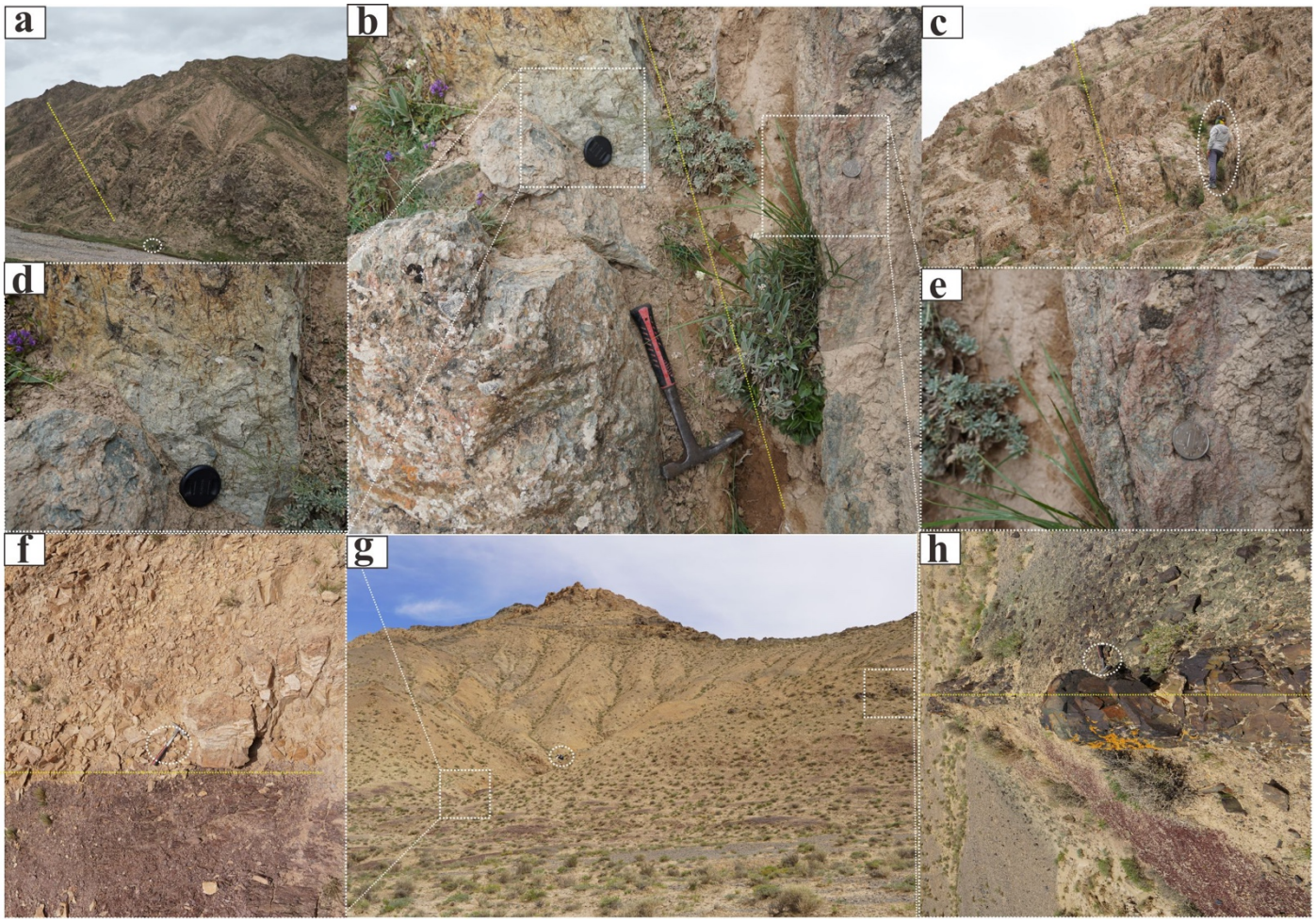

Figure S1.

Representative field photographs of sampling outcrops. (a-e) Volcanic rock of the Elashan Formation from the Hacipushan section; (f-h) The intrusive rocks from the Shihuigou section. The geologist in Fig. S1 (c, g) is about 175 cm tall; the geological hammer in Fig. S2 (b, f, h) is about 35cm in length.

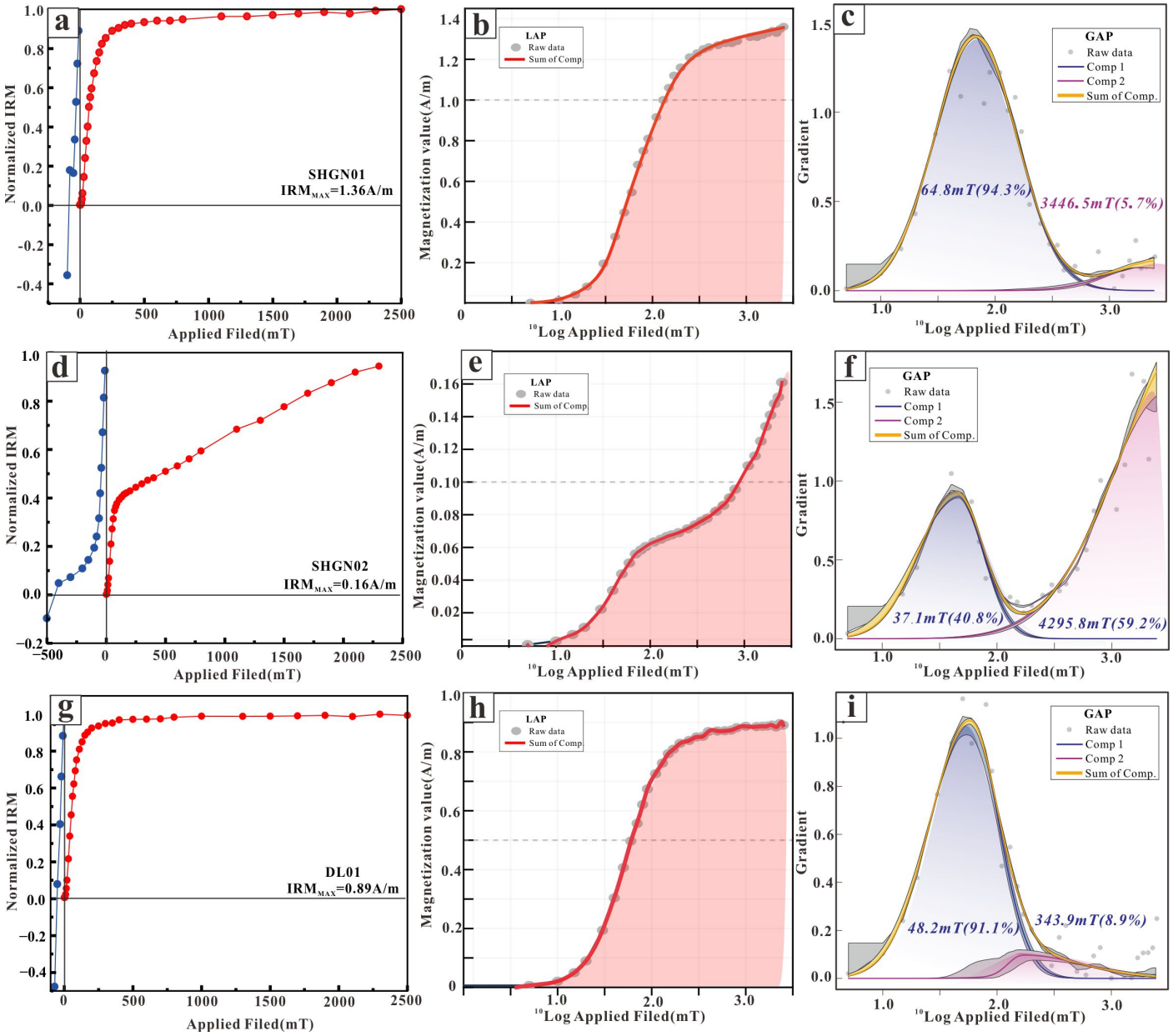

Figure S2.

Rock magnetic analyses of representative samples from this study. (a, d, g) IRM acquisition curves and backfield demagnetization of SIRM curves of representative samples; (b, d, h) LAP curves and (c, f, i) GAP curves from Cumulative Log Gaussian analysis based on the IRM curves, respectively.

Table S1 Laser ablation inductively coupled plasma spectrometry (LA-ICP-MS) data of zircons from the Hacipushan Section.

Analysis	Isotoperatios								Ages								Concor.
	Pb^{207}/Pb^{206}	1σ	Pb^{207}/U^{235}	1σ	Pb^{206}/U^{238}	1σ	Pb^{208}/Th^{232}	1σ	Pb^{207}/Pb^{206}	1σ	Pb^{207}/U^{235}	1σ	Pb^{206}/U^{238}	1σ	Pb^{208}/Th^{232}	1σ	
23DL03-040	0.0525	0.0017	0.2620	0.0083	0.0362	0.0008	0.0110	0.0003	305.6	69.98	236.2	6.64	229.3	4.84	221.8	4.91	97%
23DL03-028	0.0525	0.0017	0.2624	0.0084	0.0363	0.0008	0.0109	0.0002	305.3	70.53	236.6	6.72	229.8	4.87	219.6	4.7	97%
23DL03-039	0.0524	0.0017	0.2623	0.0085	0.0363	0.0008	0.0107	0.0002	301	72.38	236.5	6.87	230	4.87	215	4.69	97%
23DL03-002	0.0523	0.0025	0.2618	0.0125	0.0364	0.0008	0.0121	0.0003	296.2	106	236.1	10.05	230.2	5.16	243.6	6.76	97%
23DL03-030	0.0514	0.0016	0.2584	0.0081	0.0365	0.0008	0.0112	0.0003	258.4	70.23	233.4	6.54	230.9	4.88	225.4	5.16	99%
23DL03-025	0.0514	0.0019	0.2584	0.0095	0.0365	0.0008	0.0119	0.0003	256.4	82.03	233.4	7.6	231.2	5.0	238.6	5.8	99%
23DL03-036	0.0526	0.0016	0.2654	0.0080	0.0366	0.0008	0.0106	0.0002	312.6	66.58	239.0	6.4	231.6	4.9	212.9	4.3	97%
23DL03-020	0.0536	0.0018	0.2701	0.0093	0.0366	0.0008	0.0112	0.0003	352.2	75.63	242.8	7.43	231.7	4.96	225.7	5.24	95%
23DL03-006	0.0530	0.0026	0.2674	0.0132	0.0366	0.0008	0.0121	0.0004	329.7	108.43	240.6	10.6	231.7	5.2	243.7	7.01	96%
23DL03-018	0.0517	0.0016	0.2612	0.0082	0.0367	0.0008	0.0114	0.0003	271.9	69.87	235.6	6.60	232.1	4.92	228.1	5	99%
23DL03-038	0.0502	0.0015	0.2541	0.0076	0.0367	0.0008	0.0108	0.0002	206	67.91	229.9	6.18	232.2	4.87	216.4	4.51	99%
23DL03-016	0.0512	0.0016	0.2595	0.0080	0.0368	0.0008	0.0113	0.0003	251.7	68.65	234.3	6.44	232.6	4.92	226.5	4.93	99%
23DL03-033	0.0538	0.0034	0.2730	0.0171	0.0368	0.0009	0.0112	0.0004	364.1	136.4	245.1	13.6	232.8	5.52	225.8	8.76	95%
23DL03-032	0.0498	0.0028	0.2530	0.0141	0.0368	0.0009	0.0108	0.0003	187.3	126.51	229	11.45	233.1	5.37	216.3	6.53	98%
23DL03-035	0.0517	0.0016	0.2624	0.0081	0.0368	0.0008	0.0111	0.0002	270	68.49	236.6	6.47	233.2	4.91	222.3	4.74	99%
23DL03-031	0.0505	0.0015	0.2569	0.0078	0.0369	0.0008	0.0108	0.0002	217.3	68.6	232.1	6.32	233.6	4.91	216.8	4.58	99%
~~23DL03-010~~	~~0.0606~~	~~0.0020~~	~~0.3089~~	~~0.0104~~	~~0.0370~~	~~0.0008~~	~~0.0132~~	~~0.0003~~	~~625.7~~	~~70.81~~	~~273.4~~	~~8.07~~	~~234.1~~	~~5.05~~	~~264.3~~	~~5.99~~	~~85%~~
23DL03-023	0.0526	0.0017	0.2683	0.0087	0.0371	0.0008	0.0114	0.0002	309.2	71.36	241.4	6.93	234.5	4.98	228.5	4.89	97%
23DL03-027	0.0531	0.0020	0.2731	0.0104	0.0373	0.0008	0.0111	0.0003	331.2	84.41	245.1	8.33	236.3	5.05	223.4	5.08	96%
23DL03-014	0.0533	0.0032	0.2743	0.0164	0.0374	0.0009	0.0116	0.0004	340	129.72	246.2	13.0	236.5	5.3	233	7.17	96%
23DL03-022	0.0516	0.0018	0.2658	0.0094	0.0374	0.0008	0.0115	0.0003	266.3	78.72	239.3	7.50	236.6	5.07	230.8	5.51	99%
23DL03-009	0.0523	0.0018	0.2701	0.0096	0.0375	0.0008	0.0121	0.0003	300.2	78.11	242.8	7.7	237.0	5.1	242.2	5.46	98%
23DL03-019	0.0519	0.0016	0.2677	0.0084	0.0375	0.0008	0.0118	0.0003	279.5	69.97	240.9	6.75	237	5.03	236.6	5.2	98%
23DL03-001	0.0523	0.0019	0.2701	0.0098	0.0375	0.0008	0.0120	0.0003	298.2	80.25	242.8	7.82	237.2	5.13	241.7	5.84	98%
23DL03-021	0.0490	0.0017	0.2533	0.0090	0.0375	0.0008	0.0109	0.0003	147.3	80.99	229.2	7.27	237.4	5.08	218.9	5.29	96%
~~23DL03-026~~	~~0.0774~~	~~0.0033~~	~~0.4016~~	~~0.0167~~	~~0.0376~~	~~0.0009~~	~~0.0158~~	~~0.0004~~	~~1131.6~~	~~81.84~~	~~342.8~~	~~12.1~~	~~238.2~~	~~5.4~~	~~316.3~~	~~8.45~~	~~64%~~
23DL03-017	0.0546	0.0017	0.2833	0.0088	0.0377	0.0008	0.0118	0.0003	395.8	66.88	253.3	6.96	238.2	5.05	237.6	5.1	94%
23DL03-034	0.0546	0.0024	0.2831	0.0123	0.0376	0.0009	0.0118	0.0003	393.9	95.12	253.1	9.8	238.2	5.3	237	6.48	94%
23DL03-012	0.0523	0.0021	0.2718	0.0108	0.0377	0.0008	0.0120	0.0003	298.7	88.72	244.1	8.65	238.6	5.22	240.2	5.85	98%

23DL03-011	0.0498	0.0016	0.2591	0.0084	0.0378	0.0008	0.0119	0.0003	184.7	73.3	233.9	6.78	239	5.08	239.9	5.27	98%
23DL03-008	0.0534	0.0016	0.2782	0.0086	0.0378	0.0008	0.0120	0.0003	346.1	67.51	249.2	6.81	239.2	5.08	241.8	5.34	96%
23DL03-007	0.0526	0.0018	0.2750	0.0095	0.0379	0.0008	0.0128	0.0003	310.8	76.15	246.6	7.54	240.1	5.16	256.3	6.3	97%
23DL03-004	0.0519	0.0027	0.2716	0.0141	0.0380	0.0009	0.0117	0.0004	280.3	115.38	243.9	11.24	240.3	5.48	235.6	7.55	99%
23DL03-013	0.0519	0.0022	0.2717	0.0112	0.0380	0.0009	0.0115	0.0003	279.7	92.19	244.0	9.0	240.4	5.3	231.8	6.09	99%
23DL03-024	0.0536	0.0023	0.2812	0.0118	0.0381	0.0009	0.0122	0.0003	353.6	92.89	251.6	9.4	240.9	5.3	244.8	6.32	96%
23DL03-029	0.0501	0.0019	0.2631	0.0100	0.0381	0.0008	0.0116	0.0003	200.6	85.97	237.2	8.0	240.9	5.2	232.8	5.89	98%
23DL03-003	0.0509	0.0017	0.2672	0.0091	0.0381	0.0008	0.0127	0.0003	234.8	75.87	240.4	7.25	241.1	5.17	254.2	5.99	100%
23DL03-015	0.0533	0.0017	0.2803	0.0091	0.0382	0.0008	0.0118	0.0003	339.8	71.32	250.9	7.2	241.6	5.15	236.5	5.43	96%
23DL03-005	0.0523	0.0017	0.2782	0.0091	0.0386	0.0008	0.0128	0.0003	296.8	72.21	249.2	7.22	244.3	5.21	257.2	6.11	98%
~~23DL03-037~~	~~0.1500~~	~~0.0037~~	~~0.8654~~	~~0.0216~~	~~0.0418~~	~~0.0009~~	~~0.0280~~	~~0.0006~~	~~2346.3~~	~~41.82~~	~~633.1~~	~~11.73~~	~~264.2~~	~~5.56~~	~~557.9~~	~~10.91~~	~~18%~~

Table S2 Laser ablation inductively coupled plasma spectrometry (LA-ICP-MS) data of zircons from the Shihuigou Section.

Analysis	Isotoperatios								Ages								Concor.
	Pb^{207}/Pb^{206}	1σ	Pb^{207}/U^{235}	1σ	Pb^{206}/U^{238}	1σ	Pb^{207}/Th^{232}	1σ	Pb^{207}/Pb^{206}	1σ	Pb^{207}/U^{235}	1σ	Pb^{206}/U^{238}	1σ	Pb^{207}/Th^{232}	1σ	
23SHGNG02-021	0.05022	0.000735	0.25727	0.003995	0.03715	0.000435	0.01118	0.000125	205.3	33.295	232.5	3.23	235.2	2.705	224.7	2.505	99%
~~23SHGNG02-019~~	~~0.0769~~	~~0.0010~~	~~0.4166~~	~~0.0058~~	~~0.0393~~	~~0.0005~~	~~0.0131~~	~~0.000130~~	~~1119~~	~~25.165~~	~~353.6~~	~~4.14~~	~~248.4~~	~~2.85~~	~~263.5~~	~~2.59~~	~~65%~~
~~23SHGNG02-009~~	~~0.06592~~	~~0.00076~~	~~0.4808~~	~~0.0062~~	~~0.0529~~	~~0.0006~~	~~0.0177~~	~~0.000180~~	~~803.9~~	~~23.765~~	~~398.6~~	~~4.3~~	~~332.3~~	~~3.8~~	~~354.6~~	~~3.54~~	~~82%~~
~~23SHGNG02-028~~	~~0.06782~~	~~0.00084~~	~~0.49702~~	~~0.006415~~	~~0.05315~~	~~0.00058~~	~~0.01714~~	~~0.000170~~	~~863.2~~	~~25.21~~	~~409.7~~	~~4.35~~	~~333.8~~	~~3.56~~	~~343.4~~	~~3.355~~	~~80%~~
~~23SHGNG02-017~~	~~0.06642~~	~~0.00078~~	~~0.50926~~	~~0.006595~~	~~0.05561~~	~~0.000645~~	~~0.01692~~	~~0.000165~~	~~819.7~~	~~24.085~~	~~417.9~~	~~4.435~~	~~348.9~~	~~3.945~~	~~339.1~~	~~3.32~~	~~82%~~
23SHGNG02-005	0.05764	0.00069	0.44583	0.005955	0.05609	0.00066	0.01624	0.000165	516	26.07	374.4	4.185	351.8	4.035	325.5	3.24	94%
23SHGNG02-030	0.0561	0.0008	0.4354	0.0061	0.0563	0.0006	0.0171	0.00018	455.5	29.585	367	4.32	353	3.775	342.7	3.6	96%
23SHGNG02-027	0.05348	0.00082	0.4175	0.0065	0.0566	0.0006	0.01679	0.0002	349.2	33.84	354.3	4.7	355.0	3.8	336.6	3.96	100%
23SHGNG02-018	0.05776	0.00153	0.4521	0.0121	0.0568	0.0007	0.01795	0.00026	520.6	56.145	378.8	8.4	356.0	4.3	359.6	5.13	94%
23SHGNG02-031	0.0534	0.0007	0.4205	0.0059	0.0571	0.0006	0.0160	0.000175	347.4	29.925	356.4	4.19	357.7	3.82	320.1	3.43	100%
23SHGNG02-029	0.05423	0.0008	0.42882	0.00649	0.05734	0.000635	0.01646	0.00018	380.5	32.425	362.3	4.615	359.5	3.87	329.9	3.62	99%
23SHGNG02-016	0.05584	0.000825	0.44718	0.00701	0.05809	0.000685	0.01825	0.000215	445.6	32.11	375.3	4.92	364	4.185	365.6	4.275	97%
23SHGNG02-015	0.05604	0.0009	0.44909	0.007565	0.05813	0.000695	0.01712	0.00022	453.4	34.915	376.6	5.3	364.2	4.225	343	4.36	97%
23SHGNG02-010	0.0558	0.0009	0.4504	0.0073	0.0585	0.0007	0.0180	0.0002	444.5	33.21	377.5	5.10	366.7	4.245	360.1	3.925	97%
23SHGNG02-032	0.0524	0.0007	0.4239	0.0058	0.0587	0.0006	0.0171	0.000185	301.3	29.57	358.8	4.15	367.7	3.915	343.2	3.645	98%
23SHGNG02-007	0.0546	0.0007	0.4424	0.0061	0.0588	0.0007	0.0177	0.00019	394.6	27.26	372	4.28	368.3	4.22	353.8	3.82	99%
23SHGNG02-011	0.05462	0.00066	0.4437	0.0059	0.0589	0.0007	0.01761	0.000185	396.9	26.48	372.9	4.2	369.0	4.2	352.8	3.705	99%
23SHGNG02-003	0.05564	0.00104	0.45217	0.008745	0.05893	0.00072	0.01818	0.00026	437.9	40.55	378.8	6.115	369.1	4.39	364.2	5.21	97%
23SHGNG02-014	0.0537	0.000715	0.4374	0.0063	0.0591	0.0007	0.01785	0.000195	358.4	29.515	368.4	4.5	370.0	4.2	357.5	3.895	100%
23SHGNG02-008	0.0554	0.0008	0.4520	0.0071	0.0591	0.0007	0.0176	0.000195	429.3	31.69	378.7	4.93	370.4	4.285	352.4	3.88	98%
23SHGNG02-006	0.05434	0.00073	0.44307	0.006465	0.05914	0.0007	0.01757	0.0002	385	29.5	372.4	4.55	370.4	4.265	352	3.975	99%
23SHGNG02-020	0.0536	0.0007	0.4400	0.0062	0.0595	0.0007	0.0188	0.0002	354.9	29.17	370.2	4.41	372.7	4.22	375.8	3.935	99%
23SHGNG02-001	0.05555	0.00074	0.45685	0.006655	0.05965	0.00071	0.0188	0.000215	434.1	29.04	382.1	4.64	373.5	4.31	376.6	4.3	98%
23SHGNG02-024	0.06014	0.001125	0.49737	0.009545	0.05999	0.000725	0.01933	0.000245	608.5	39.45	409.9	6.475	375.5	4.405	386.9	4.87	91%
23SHGNG02-026	0.0538	0.0007	0.4482	0.0059	0.0605	0.0007	0.0190	0.000195	360.3	28.115	376	4.17	378.6	4.025	380.1	3.88	99%
23SHGNG02-023	0.0541	0.0007	0.4508	0.0065	0.0605	0.0007	0.0185	0.000195	373.2	29.7	377.8	4.57	378.6	4.28	370.3	3.88	100%
23SHGNG02-002	0.05372	0.00074	0.4497	0.0067	0.0607	0.0007	0.01893	0.000225	359	30.38	377.1	4.7	380.0	4.4	378.9	4.42	99%
23SHGNG02-004	0.0544	0.0006	0.4569	0.0060	0.0610	0.0007	0.0189	0.0002	385.4	25.605	382.1	4.16	381.5	4.36	378.1	3.93	100%
23SHGNG02-022	0.0540	0.0011	0.4939	0.0101	0.0663	0.0008	0.0198	0.00025	372.1	43.62	407.6	6.88	413.8	4.865	396.1	4.995	98%

23SHGNG02-025	0.0665	0.0008	1.1700	0.0143	0.1275	0.0014	0.0390	0.000455	823.4	23.805	786.6	6.71	773.7	7.955	772.5	8.87	98%
23SHGNG02-013	0.11982	0.001355	5.6445	0.0714	0.3417	0.0040	0.10085	0.001005	1953.5	19.915	1922.9	10.9	1894.8	19.3	1942	18.41	99%
23SHGNG02-012	0.1770	0.0018	9.9678	0.1178	0.4084	0.0048	0.1595	0.00155	2625.2	16.875	2431.8	10.91	2207.6	21.75	2991.9	27.025	90%

Table S3 ChRM directions for Middle Triassic volcanic rocks in the Qaidam Basin.

Site	Lat. (° N)	Long. (° E)	Strike/dip	n/N	D_g (°)	I_g (°)	D_s (°)	I_s (°)	k	α_{95} (°)	VGP	
											Λ (°N)	Φ (°E)
The intrusive rocks from the south of Shihuigou County (~235Ma)												
SHGN1	37°22.017′	96°6.350′	92/34	6/10	43.2	26.14	65.98	45.68	30.91	12.24	34.37	176.18
SHGN2	37°22.017′	96°6.350′	92/34	5/9	32.78	21.02	47.82	48.23	47.87	11.17	49.65	183.22
SHGN3	37°22.017′	96°6.350′	67/44	7/8	359.22	16.06	16.07	54.78	43.69	9.23	76.91	190.3
SHGN4	37°22.017′	96°6.350′	67/44	7/8	358.56	17.76	16.45	56.59	59.07	7.92	76.92	181.99
SHGN5	37°22.017′	96°6.350′	67/44	4/5	17.24	29.09	64.53	63.21	177.77	6.91	42.06	155.88
SHGN6	37°22.017′	96°6.350′	77/51	7/9	17.8	32.68	71.98	63.25	70.63	7.23	37.01	153.83
Mean				**6**	**16.18**	**24.35**	**44.70**	**57.63**	**20.17**	**5.45**	**55.03**	**170.57**
The volcanic rocks from the east of Dulan County (~235.6Ma)												
DL1	36°16.452′	98°25.464′	300/36	6/10	239.35	-71.03	221.47	-36.76	60.63	8.67	-50.62	20.75
DL2	36°16.452′	98°25.464′	300/36	10/10	264.24	-77.16	224.89	-45.44	245.29	3.09	-51	9.43
DL3	36°16.452′	98°25.464′	300/36	10/10	281.25	-78.93	226.17	-49.26	101.84	4.81	-51.25	364.02
DL4	36°16.452′	98°25.464′	300/36	8/10	312.92	-66.2	250.25	-52.49	269.01	3.38	-33.45	349.58
DL5	36°16.452′	98°25.464′	300/36	8/9	312.7	-67.96	247.44	-52.98	83.42	6.1	-35.78	350.22
DL6	36°16.452′	98°25.464′	300/36	8/10	311.59	-67.12	248.54	-52.3	230.63	3.66	-34.68	350.49
Mean				**6**	**293.35**	**-73.75**	**235.21**	**-49.26**	**47.57**	**2.95**	**-44.01**	**359.61**
The volcanic rocks from the northeast of Dulan County (~237Ma) (Wang et al., 2024)												
DLTB11	36°21.743′	98°12.282′	198/24	7/8	70.7	39	51.3	55.7	124.1	5.4	49.2	172.5
DLTB12	36°21.743′	98°12.282′	198/24	7/10	59.3	31.1	43.5	44.6	32.5	10.8	51.8	191
DLTB13	36°21.743′	98°12.282′	198/24	10/10	62	33.3	45.1	47.6	81.9	5.4	51.6	186.4
DLTB14	36°21.743′	98°12.282′	198/24	4/9	67.9	40.3	46.7	55.9	44.7	13.9	52.8	173.8
DLTB15	36°21.743′	98°12.282′	198/24	9/9	59.6	38.5	38.7	51.3	54.7	7	57.9	184.6
DLTB16	36°21.743′	98°12.282′	198/24	8/8	61.7	40	39.8	53.4	165.6	4.3	57.6	180.5
DLTB17	36°21.743′	98°12.282′	198/24	9/13	55	36.7	35.2	48	67.5	6.3	59.7	192
DLTB18	36°21.743′	98°12.282′	198/24	10/11	54.1	36.4	34.4	47.3	369	2.5	60.1	193.6
DLTB19	36°21.743′	98°12.282′	198/24	5/10	68.8	41.6	46.8	57.4	85.5	8.3	53.1	171.2
DLTB20	36°21.743′	98°12.282′	198/24	6/11	61.9	37.2	42.3	50.9	87.4	7.2	54.9	183.4
DLTB21	36°21.743′	98°12.282′	198/24	5/9	63.8	24	52.2	39.6	33	13.5	43.1	190.4
DLTB22	36°21.743′	98°12.282′	198/24	4/8	72.5	40.4	52.4	57.6	83.3	10.1	48.9	169.2

DLT1	36°21.866′	98°12.012′	205/40	6/9	83.2	30	53.1	58.9	177.1	5	48.7	167
DLT2	36°21.866′	98°12.012′	205/40	4/5	84	29.6	54.5	59.1	509.1	4.1	47.7	166.3
DLT4	36°21.866′	98°12.012′	205/40	3/9	81.7	31.2	49.6	58.9	130.9	10.8	51.3	167.8
DLT5	36°21.866′	98°12.012′	205/40	4/10	81.3	31.2	49.2	58.7	768	3.3	51.5	168.3
DLT6	36°21.866′	98°12.012′	205/40	3/8	81	34.8	43.8	61	802.7	4.4	56	164.9
DLT7	36°21.866′	98°12.012′	205/40	3/8	85.7	36.2	46.9	64.8	217.8	8.4	54	156.6
DLT8	36°21.866′	98°12.012′	205/40	4/9	83.3	30.9	51.9	59.6	479.3	4.2	49.7	166.1
DLT9	36°21.866′	98°12.012′	205/40	4/10	81.9	31.8	49.1	59.4	1101	2.7	51.8	167.1
DLT10	36°21.866′	98°12.012′	205/40	9/11	81.8	29.9	51.4	58	86.6	5.6	49.7	168.9
Mean				**21**	**71.2**	**35.2**	**46**	**54.6**	**122.6**	**3**	**53**	**176.1**
The volcanic rocks from the Wutumeiren (~242Ma) (Wang et al., 2024)												
WD2	36°43.788′	93°31.681′	251/31	7/8	241.8	-67.3	196.8	-49.3	86.1	6.5	-74.6	23.6
WD3	36°43.788′	93°31.681′	251/31	7/7	258.5	-69.5	199.1	-55.7	221.2	4.1	-74.7	359.5
WD4	36°43.788′	93°31.681′	251/31	4/8	248.2	-66.7	199.9	-51.1	197.5	6.6	-72.9	14.3
WD6	36°43.788′	93°31.681′	251/31	4/10	252	-61.2	208.4	-49.0	119.1	8.5	-65.4	11.2
WD7	36°43.788′	93°31.681′	251/31	7/11	249.2	-58.6	213.4	-44.9	63.3	10.5	-60.0	13.7
GEM8	36°43.788′	93°31.681′	251/31	4/8	216.4	-64.6	188.7	-40.4	120	8.4	-74.4	62.3
GEM10	36°43.788′	93°31.681′	251/31	7/12	257	-65.2	205.1	-53.2	119.4	5.5	-69.3	4.2
Mean				**7**	**246.2**	**-65.3**	**201.5**	**-49.4**	**115.2**	**5.6**	**71**	**197**
Mean（All sections）				**40**	**63.67°±9.91°**	**47.03°±10.44°**	**43.25°±4.94°**	**54.23°±4.10°**	**K=7.71 K=32.1**	**A95=8.72 A95=4.05**	**54.01**	**183.68**

Note. Strike/Dip = right-hand strike/dip of the strata; n/N = number of samples used to calculate mean/total samples demagnetized; D/I = declination/inclination; k/K = the precision parameter; α_{95}/A95 = the radius that the mean direction lies within 95% confidence; Plat/Plon = latitude/longitude of paleopoles. The final mean results are calculated using the reference site (36.27°N, 98.64°E).

(1) The fold test is inconclusive at the 95% and 99% confidence (McElhinny & Opdyke, 1964): Ks/Kg = 5.22259 < F(2(n2-1),(n1-1)) at 5% and 1% point = 1.4569 and 1.7140, respectively;*

(2) The fold test is positive at the 95% and 99% confidence (McFadden, 1990), critical Xi at 95% = 7.264, Xi at 99% = 10.27; Xi1 IS = 31.02, Xi1 TC = 6.684; Xi2 IS = 34.49, Xi2 TC = 2.353.

(3) The fold test (Tauxe & Watson, 1994), the highest τ is between [82%,102%] unfolding.

(4) Reversal test (McFadden and McElhinny 1990), angle between the two averages γ = 7.3° > γcritical = 7.0° indicates a B class result.

(5) Reversal test (Tauxe, 2010), 1000 bootstrapped Cartesian coordinates for the collections at 95% confidence are matched.

(6) Common Mean Direction Test (CMDT) (Heslop et al., 2023), CMDT value=14.59; CMDT critical value=18.43; CMDT p-value=0.09. This result showed a match.

Table S4 Compilation of Permo-Triassic Palaeomagnetic Poles from the Qaidam, North China, North Qiangtang and Tarim (reference site: 36.27°N, 98.64°E)

Number	Name	Age	Min_age	Max_age	Slat	Slon	N	K	A95	Plat	Plon	Mdec	Minc	Lithology	f	Paleolatitude	Reference
1	**Qaidam**	238	234.1	241.9	36.27	98.64	40	32.10	4.05	54.01	183.68	43.25	50.58	**V**		31.31	*This study*
2	**Qaidam**	239.3	237	241.5	36.45	98.28	28	44.4	4.1	57.99	179.86	39.5	53.95	V		34.53	*(Wang et al., 2024)*
3	**Qaidam**	255.7	251.9	259.5	37.5	99.1	199	26.1	2.0	77.43	331.17	348.66	48.2	C	0.63	28.08	*(T. Wang et al., 2025)*
4	**Kunlun- Qaidam**	258	251.4	264.6	36.07	94.82	42	45.29	3.31	81.59	267.22	1.88	46.77	V		27.33	*(Song et al.,2026)*
1	**North China**	174	168	180	42.08	117.94	28	10.86	8.67	70.26	143.68	16.52	73.24	V		48.52	*(Yi et al.,2019)*
2	**North China**	248.5	246	251.9	40.80	118.50	21	28.6	6	53.24	9.41	322.4	39	C	0.48	28.71	*(Zhao et al.,2020)*
3	**North China**	248.5	246	251	36.00	112.40	15	32.5	6.8	52.51	15.75	318.5	41.9	C	0.6	32.01	*(Zhou et al.,2018)*
4	**North China**	255	251.9	259.5	42.50	119.20	14	148	3.3	54.33	19.16	319.3	47.1	V		34.50	*(Ren et al.,2020)*
5	**Alxa**	255	254	256	39.64	101.07	8	108.57	5.34	82.03	291.79	358.26	51.11	C&V		28.49	*(Xu et al.,2025)*
6	**North China**	266.5	259	274	43.20	119.00	14	15.2	10.6	71.79	336.69	347.5	46.8	V		25.38	*(Zhao et al.,1990)*
7	**Alxa**	268	264	272	39.64	101.01	17	31.77	6.43	40.02	4.28	305.99	35.97	V		19.48	*(Xu et al.,2025)*
8	**North China**	274	268	280	42.00	114.00	24	54.4	4.1	65.39	326.74	346.1	36.6	V		18.28	*(Zhang et al.,2018)*
9	**Alxa**	282.5	282	283	39.62	101.60	22	23.8	6.49	48.8	357.13	317.03	37.04	V		19.83	*(Xu et al.,2025)*
10	**North China**	285	274.4	298.9	41.20	112.20	51	17.01	4.98	44.08	9.63	311.78	35.93	V+C	0.7	24.93	*(Ren et al.,2025)*
1	**Amuria**	219	237	201	43.7	118.8	15	50.05	4.6	70.4	233.8	21.2	39.0	C	0.6	33.3	*(Zhao et al.,2023)*
2	**Amuria**	187.75			51.1	106.8	6	8.89	23.64	43.29	131.38	98.46	75.62	V		52	*(Cognéet al.,2005)*
1	**Tarim**	287.6	284.9	290.3	40.8	79.75	72	28.2	3.2	50.91	171.12	46.54	48.78	V+C		37.75	*(Wei et al., 2020)*

Note. Min_age/Max_age = lower and upper boundaries of age uncertainty range (in Ma); Slat/Slon = latitude and longitude of (mean) sampling location; N = number of paleomagnetic sites used to compute the paleopole; K=Fisher (1953) precision parameter of the distribution of virtual geomagnetic poles (VGPs); A95 = radius of the 95% confidence circle about the paleopole; Plat/Plon = paleopole latitude and longitude; Mdec/Minc = mean declination and inclination; f = flattening factor (only for sedimentary data) (Cogné et al., 2005,Ren et al., 2025, 2020; Song et al., 2026; Wang et al., 2024, 2025;Wei et al.,2020; Xu et al., 2025; Yi et al., 2019; Zhang et al., 2018; Zhao et al., 2023, 2020, 1990; Zhou et al., 2018)

Table S5: Evaluation of the Noth China and North Qiangtang poles relative to the reference APWP using weighted uncertainties

Number	Age	Min_age	Max_age	Plat	Plon	A_{95}	Paleolatitude	Reference
APWP of the North China Block								
1	170	162.5	177.5	70.17	143.31	8.74	48.7	This study
2	180	172.5	187.5	70.64	143.65	11.35	48.4	This study
3	240	232.5	247.5	52.46	10.83	8.44	29.2	This study
4	250	242.5	257.5	58.02	10.67	2.71	31.2	This study
5	260	252.5	267.5	63.08	3.38	6.10	29.6	This study
6	270	262.5	277.5	57.46	349.85	3.68	21.1	This study
7	280	272.5	287.5	53.21	353.04	3.58	20.2	This study
8	290	282.5	297.5	44.79	1.84	6.34	20.5	This study

Note. Min_age/Max_age = lower and upper boundaries of age uncertainty range (in Ma); Plat/Plon = paleopole latitude and longitude; A95 = radius of the 95% confidence circle about the paleopole Mdec/Minc = mean declination and inclination; f = flattening factor (only for sedimentary data)

References

Chai, R.Y., Zhou, Y.N., Wang, T., Cheng, X., Wei, B.T., Jiang, N., et al. (2024). New Rock Magnetism and Magnetic Fabrics Studies on the Late Triassic Volcanic Rocks from Qaidam Block, Northern Tibetan Plateau. Minerals, 14(5), 515. https://doi.org/10.3390/min14050515

Cogné, J.-P., Kravchinsky, V. A., Halim, N., & Hankard, F. (2005). Late Jurassic-Early Cretaceous closure of the Mongol-Okhotsk Ocean demonstrated by new Mesozoic palaeomagnetic results from the Trans-Baïkal area (SE Siberia). Geophysical Journal International, 163(2), 813–832. https://doi.org/10.1111/j.1365-246X.2005.02782.x

Egli, R. (2003). Analysis of the field dependence of remanent magnetization curves. Journal of Geophysical Research: Solid Earth, 108(B2), 2002JB002023. https://doi.org/10.1029/2002JB002023

Fisher, R. (1953). Dispersion on a Sphere. Proceedings of the Royal Society A: Mathematical, Physical and Engineering Sciences, 217(1130), 295–305. https://doi.org/10.1098/rspa.1953.0064

Heslop, D., Dekkers, M. J., Kruiver, P. P., & Van Oorschot, I. H. M. (2002). Analysis of isothermal remanent magnetization acquisition curves using the expectation-maximization algorithm. Geophysical Journal International, 148(1), 58–64. https://doi.org/10.1046/j.0956-540x.2001.01558.x

Heslop, David, Scealy, J. L., Wood, A. T. A., Tauxe, L., & Roberts, A. P. (2023). A Bootstrap Common Mean Direction Test. Journal of Geophysical Research: Solid Earth, 128(8), e2023JB026983. https://doi.org/10.1029/2023JB026983

Kirschvink, J. L. (1980). The least-squares line and plane and the analysis of palaeomagnetic data. Geophysical Journal International, 62(3), 699–718. https://doi.org/10.1111/j.1365-246X.1980.tb02601.x

Koymans, M. R., Van Hinsbergen, D. J. J., Pastor-Galán, D., Vaes, B., & Langereis, C. G. (2020). Towards FAIR Paleomagnetic Data Management Through Paleomagnetism.org 2.0. Geochemistry, Geophysics, Geosystems, 21(2), e2019GC008838. https://doi.org/10.1029/2019GC008838

Koymans, Mathijs R., Langereis, C. G., Pastor-Galán, D., & Van Hinsbergen, D. J. J. (2016). Paleomagnetism.org: An online multi-platform open source environment for paleomagnetic data analysis. Computers & Geosciences, 93, 127–137. https://doi.org/10.1016/j.cageo.2016.05.007

Kruiver, P. P., Dekkers, M. J., & Heslop, D. (2001). Quantification of magnetic coercivity components by the analysis of acquisition curves of isothermal remanent magnetisation. Earth and Planetary Science Letters, 189(3–4), 269–276. https://doi.org/10.1016/S0012-821X(01)00367-3

McElhinny, M. W., & Opdyke, N. D. (1964). The paleomagnetism of the precambrian dolerites of Eastern Southern Rhodesia, an example of geologic correlation by rock magnetism. Journal of Geophysical Research, 69(12), 2465–2475. https://doi.org/10.1029/JZ069i012p02465

McFadden, P. L. (1990). A new fold test for palaeomagnetic studies. Geophysical Journal International, 103(1), 163–169. https://doi.org/10.1111/j.1365-246X.1990.tb01761.x

Ren, Q., Zhang, S.H., Gao, Y.J., Zhao, H.Q., Wu, H.C., Yang, T.S., & Li, H.Y. (2020). New Middle–Late Permian Paleomagnetic and Geochronological Results From Inner Mongolia and their Paleogeographic Implications. Journal of Geophysical Research: Solid Earth, 125(7), e2019JB019114. https://doi.org/10.1029/2019JB019114

Ren, Q., Zhang, S.H., Hou, M.C., Zheng, D.Y., Wu, H.C., Yang, T.S., et al. (2025). Continental drift triggered the Early Permian aridification of North China. Nature Communications, 16(1), 384. https://doi.org/10.1038/s41467-024-55804-8

Song, P.P., Ding, L., Zhang, L., Wu, C., Duan, X.Y., Yue, Y.H., & Xie, J. (2026). Defining the main Paleo-Tethys suture in Tibet: First Permian paleomagnetic insights from the Eastern Kunlun Range. Earth and Planetary Science Letters, 681, 119925. https://doi.org/10.1016/j.epsl.2026.119925

Tauxe, L., & Watson, G. S. (1994). The fold test: an eigen analysis approach. Earth and Planetary Science Letters, 122(3–4), 331–341. https://doi.org/10.1016/0012-821X(94)90006-X

Tauxe, L. (2010). Essentials of Paleomagnetism, Univ. of California Press, Berkeley. https://doi.org/10.1525/9780520946378

Wang, B., Huang, B.C., Yang, Z.Y., Zhang, G.W., Liu, X.M., Duan, L., et al. (2024). Palaeomagnetic results from Early Mesozoic strata in the Qaidam Basin and their implications for the formation of the Northern China Domain. Geophysical Journal International, 236(3), 1621–1635. https://doi.org/10.1093/gji/ggad496

Wang, T., Zhou, Y.N., Van Hinsbergen, D. J. J., Sun, J.P., Cheng, X., Chai, R.Y., et al. (2025). Paleomagnetic Evidence for a Late Permian Qaidam-North China Connection, and the Cryptic Final Mesozoic Intra-Asian Suture. Journal of

Geophysical Research: Solid Earth, 130(8), e2025JB031123. https://doi.org/10.1029/2025JB031123

Wei, B.T., Yang, X.F., Cheng, X., Domeier, M., Wu, H.N., Kravchinsky, V. A., et al. (2020). An absolute paleogeographic positioning of the early Permian Tarim large igneous province. Journal of Geophysical Research: Solid Earth, 125(5), e2019JB019111. https://doi.org/10.1029/ 2019JB019111

Xu, W., Song, B., Shi, J.Z., Li, Y., Wang, B.W., Ye, X.Z., et al. (2025). New Permian Paleomagnetic and Geochronologic Results From the Alxa Block: Constraints on Its Tectonic Affinity and the Closure of Paleo-Asian Ocean. Geophysical Research Letters, 52(20), e2025GL116752. https://doi.org/10.1029/2025GL116752

Yi, Z.Y., Liu, Y.Q., & Meert, J. G. (2019). A true polar wander trigger for the Great Jurassic East Asian Aridification. Geology, 47(12), 1112–1116. https://doi.org/10.1130/G46641.1

Zhang, D.H., Huang, B.C., Zhao, J., Meert, J. G., Zhang, Y., Liang, Y.L., et al. (2018). Permian Paleogeography of the Eastern CAOB: Paleomagnetic Constraints From Volcanic Rocks in Central Eastern Inner Mongolia, NE China. Journal of Geophysical Research: Solid Earth, 123(4), 2559–2582. https://doi.org/10.1002/2018JB015614

Zhao, P., Appel, E., & Xu, B. (2020). An Inclination Shallowing-Corrected Early Triassic Paleomagnetic Pole for the North China Craton: Implication for the Mesozoic Geography of Proto-Asia. Journal of Geophysical Research: Solid Earth, 125(10), e2020JB019489. https://doi.org/10.1029/2020JB019489

Zhao, P., Appel, E., Deng, C., & Xu, B. (2023). Bending of the Western Mongolian Blocks Initiated the Late Triassic Closure of the Mongol-Okhotsk Ocean and Formation of the Tuva-Mongol Orocline. Tectonics, 42(5), e2022TC007475. https://doi.org/10.1029/2022TC007475

Zhao, X.X., Robert S.C., Zhou, Y.X., Wu, H.R., & Wang, J. (1990). New paleomagnetic results from northern China: collision and suturing with Siberia and Kazakhstan. Tectonophysics, 181(1–4), 43–81. https://doi.org/10.1016/0040-1951(90)90008-V

Zhou, T.H., Huang, B.C., Jia, S.F., Liang, Y.L., Zhang, D.H., Zhao, Q., Zhang, Y. & Yan, Y.G. (2018). Paleomagnetic inclination shallowing in lower Triassic Liujiagou Formation from Qinshui basin, North China block, Acta Sci. Nat. Univ. Pekinensis, 54(3), 521–534. doi:10.13209/j.0479- 8023.2017.100 (in Chinese).

Zijderveld, J.D.A. (1967). The natural remanent magnetizations of the exeter volcanic traps (Permian, Europe). Tectonophysics, 4(2), 121–153. https://doi.org/10.1016/0040-1951(67)90048-0